Controls on the isotopic composition of microbial methane

Jonathan Gropp,[1*] Qusheng Jin,[2] Itay Halevy[1]

[1]Department of Earth and Planetary Sciences, Weizmann Institute of Science, Rehovot, Israel

[2]Department of Earth Sciences, University of Oregon, Eugene, Oregon, USA

[*]To whom correspondence should be addressed; E-mail: jonathan.gropp@weizmann.ac.il.

Abstract

Microbial methane production (methanogenesis) is responsible for more than half of the annual emission of this major greenhouse gas to the atmosphere. Though the stable isotopic composition of methane is often used to characterize its sources and sinks, strictly empirical descriptions of the isotopic signature of methanogenesis currently limit such attempts. We developed a biochemical-isotopic model of methanogenesis by CO_2 reduction, which predicts carbon and hydrogen isotopic fractionations, and clumped isotopologue distributions, as functions of the cell's environment. We mechanistically explain multiple-isotopic patterns in laboratory and natural settings and show that such patterns constrain the in-situ energetics of methanogenesis. Combining our model with data from environments in which methanogenic activity is energy-limited, we provide predictions for the biomass specific methanogenesis rates and the associated isotopic effects.

Introduction

Methane (CH_4) is a major greenhouse gas, with both natural and anthropogenic sources (1). The primary natural source of biogenic methane emissions is archaeal methanogenesis in anoxic environments (2), about a third of which is hydrogenotrophic (3), with the net reaction:

$$4H_2 + CO_2 \rightleftarrows CH_4 + 2H_2O\ . \tag{1}$$

Strong isotopic discrimination during biological and abiotic methane formation has motivated the use of methane hydrogen and carbon isotopes to trace its production and consumption processes, construct global methane budgets, and evaluate its climatic impacts (1, 4, 5). In early studies of the isotopic composition of methane in the environment, temperature-dependent thermodynamic isotopic equilibrium between methane and carbon dioxide was considered to be an important control on methane carbon isotopes (6–9). Contemporaneous laboratory culture experiments, in contrast, displayed methane carbon and hydrogen isotope compositions that departed from thermodynamic isotopic equilibrium (10–14). Subsequent experimental studies that empirically related the thermodynamics of microbial methanogenesis (the Gibbs free energy of the net reaction) to the associated isotopic discrimination, offered a means to reconcile the early laboratory and environmental results (15–21). Organism-level models that employ isotopic mass balance to explain the observed range of microbial isotopic discrimination in hydrogenotrophic methanogenesis have been developed (22–24), but to date, such models have prescribed rather than resolved the microbial biochemistry. It has been difficult, therefore, to distinguish between different methane sources, different modes and extents of environmental methane cycling, and different environmental controls on the microbial isotopic discrimination as drivers of observed variations in the isotopic composition of methane.

Metabolic-isotopic models link the thermodynamics and kinetics of biochemical reactions to the isotopic discrimination imparted by metabolic activity (25). To constrain the microbial component of observed variations in the carbon and hydrogen isotope composition of methane, we developed and analyzed a full metabolic-isotopic model of hydrogenotrophic methanogenesis. The model

predicts the isotopic discrimination and its relation to the energy available to drive the methanogenesis reaction and to cell-specific methanogenesis rates in laboratory cultures, providing a quantitative tool to explore the dependence of methane isotopic composition on the metabolic state of the methanogenic cells. Extending our analysis to energy-limited conditions, which are prevalent in natural environments, our model predicts the environmental and metabolic controls on the isotopic composition of methane.

Results and Discussion

Calibration and validation of a metabolic model of hydrogenotrophic methanogenesis

We constructed mass balance equations for the concentrations of the intracellular metabolites in the hydrogenotrophic methanogenesis pathway (Fig. 1A). In such a mass balance, enzymatically-catalyzed reactions in the pathway produce and consume the various metabolites at rates that are determined by reversible Michaelis-Menten type rate laws, which account for the reaction kinetics and thermodynamics (26, details in the Methods, and tables S1 and S2). We regard the 'transformed' standard-state and actual Gibbs free energies ($\Delta G_r'^0$ and ΔG_r, respectively), which are calculated at the constant pH and ionic strength that are maintained by intracellular homeostasis (27). Given fixed extracellular aqueous concentrations of CO_2, H_2 and CH_4 (henceforth denoted $[CO_2]$, $[H_2]$ and $[CH_4]$), and pH, which define the Gibbs free energy of net methanogenesis (ΔG_{net}), the mass balance equations are solved for the steady-state concentrations of the intracellular metabolites (fig. S1). At this steady state, the model links metabolite concentrations to the net rate of methanogenesis, and to the gross forward and reverse rates of the individual reactions.

Our model specifically represents methanogens that do not have membrane-associated methanophenazines. These methanogens characteristically couple ferredoxin (Fd) reduction by H_2 to the reduction of the heterodisulfide CoM-S-S-CoB by the Mvh/Hdr enzyme complex (28, table S1). Recent observations suggest that Mvh/Hdr may form a larger complex with Fmd, and that formate or coenzyme

F_{420} may serve as the electron donor for this coupled reaction instead of soluble Fd (29). We did not represent this complex in the model, as the physiological conditions under which it emerges are not yet clear. Should this complex prove to be of ecological significance, it may readily be included in future versions of our model.

We calibrated our metabolic model to available measurements of biomass-specific methanogenesis rates and their relation to $[H_2]$ in the μM to mM range (Fig. 1B). The procedure for calibrating the metabolic model parameters to obtain optimal model-measurement agreement is described in the Methods. The enzyme maximal rate capacities (V^+) required for the model are taken from crude cell extract measurements (i.e., *in-vitro*, table S2). We found that over the range of $[H_2]$ measured in culture experiments, optimal model agreement with experimental *in-vivo* results requires scaling *in-vitro* rate capacities up by a factor of $\approx$11 (fig. S2J). The necessity for such scaling may reflect different enzyme concentrations in the cell extracts compared to living cells, product buildup, and substrate depletion, among other factors (25). After model calibration to reproduce $[H_2]$-dependent biomass-specific methanogenesis rates, we next validated the model (with no further parameter tuning) against available measurements of metabolite concentrations and oxidation states.

The metabolic model accounts for electron transfer from H_2 to the intermediate metabolites through three electron carriers, F_{420}, coenzyme B (HS-CoB), and Fd, thereby providing insight into the oxidation state of the cell. We validated the model's predictions for the oxidation state of these electron carriers against available measurements (table S3). The reduction of F_{420} depends directly on $[H_2]$, and we find that F_{420} in the model is 50% reduced at $[H_2]$ of $\approx$50 μM (fig. S1K). This $[H_2]$ is higher than observed in cell suspensions (50% reduction at $[H_2]$ of $\approx$5 μM, table S3), but in line with observations in fed-batch cultures (F_{420} 65%–90% reduced at a H_2 concentration of 10 to 40 μM, Ref. 30). We note that in the model, the degree of F_{420} reduction is insensitive to variations in the kinetic parameters (V^+, and the Michaelis constants, K_M), and is only sensitive to the $\Delta G_r'^0$ of the Frh-catalyzed reaction, which was calculated using the standard reduction-oxidation potential (E'^0) of the reaction $F_{420} + 2e^- \rightarrow F_{420}H_2$ (table S4). We found that setting a $\Delta G_r'^0$ value

that is 7 kJ mol^{-1} more negative than the default model value results in a better match with the cell suspensions. However, this implies an E'^0 value for F_{420} of −320 mV, which is significantly less negative than available measurements (−373 to −353 mV, Refs. 31–33), and we adopt the $\Delta G_r'^0$ calculated with the more reasonable F_{420} E'^0 value. The model HS-CoB/CoM-S-S-CoB couple is 2–20% reduced at [H_2] of 10 μM, depending on CO_2 concentrations (fig. S1L), within the observed range of this couple's oxidation state at similar [H_2] (0.5% to 55% reduced, Ref. 34, table S3). We note that over the range of [H_2] at which the electron carrier oxidation state measurements were made, ΔG_{net} is negative enough that some of the reactions in the pathway operate in disequilibrium. Model-measurement agreement, therefore, supports that both the thermodynamic and kinetic model parameters have approximately correct values. Our observation-validated model predictions suggest that the intracellular oxidation state of electron carriers generally does not reflect electrochemical equilibrium, and is instead maintained dynamically, by oxidation and reduction fluxes that depend on the cell's metabolic activity. This dynamic control means that measurements of the oxidation state of specific reduction-oxidation couples does not necessarily bear on the oxidation state of other reduction-oxidation couples (both inorganic and organic) and on the overall oxidation state of the cell.

We also validated the model predictions against the few available measurements of metabolite concentrations. Concentrations of HS-CoM in the model vary as a function of both [H_2] and [CO_2] (fig. S1I), spanning a wide range between 3 and 200 μM at [H_2] of 10 μM and [CO_2] between 0.1 and 100 mM. Measured HS-CoM concentrations show a very similar range, 4 to 200 μM, at similar [H_2] (Ref. 35, table S3). Measured CH-H_4MPT concentrations were 13–35 μM at [H_2] of ≈1.5 mM under different growth regimes (35), in agreement with model CH-H_4MPT concentrations of ≈10–100 μM at [H_2] of 1.5 mM. Lastly, the ratio of CHO-MFR to MFR in the model ranges between 1 and 2.6 at [H_2] of 10 μM, within the lower range of this ratio measured under similar conditions (1.15 to 10, Ref. 34, table S3). As in the case of the oxidation state of electron carriers, model-measurement agreement in the case of metabolite concentrations supports that both the thermodynamic and kinetic model parameters have broadly correct values.

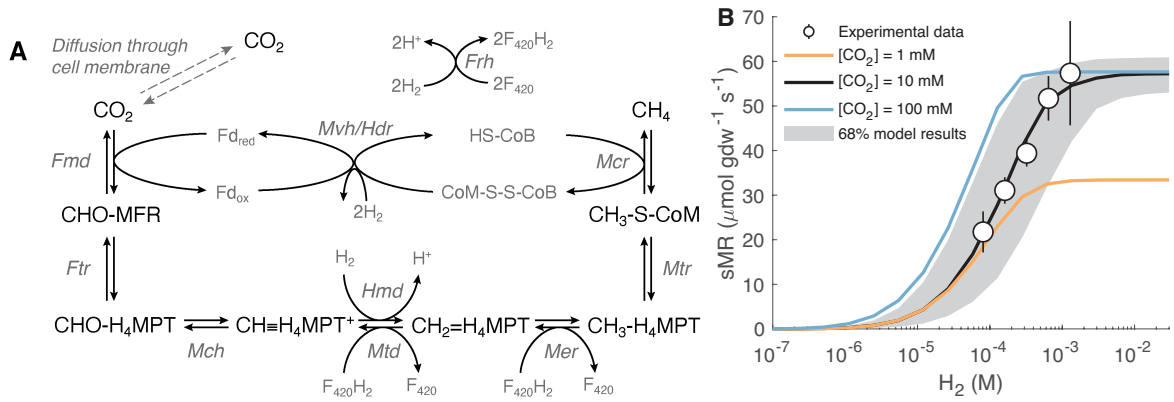

Figure 1: A metabolic model of hydrogenotrophic methanogenesis. (**A**) Schematic illustration of the metabolic pathway including all reactions that are included in the metabolic model. Abbreviated enzyme names are in italics (table S1). (**B**) Metabolic model calibration to measured biomass-specific methanogenesis rates (sMR) as a function of the H_2 concentration. Measured sMR (circles) during the linear and stationary phase in laboratory cultures of *M. thermoautotrophicus* grown at 60°C (error bars are standard deviations for four experiments, Ref. 36). The median (solid lines) of 10^3 model simulations with 1, 10, and 100 mM [CO_2] and 68% (gray envelope) of simulations with 10 mM [CO_2] are shown. The envelope represents K_M values that were drawn from posterior distributions resulting from the model calibration (see Methods, fig. S2 and table S5).

The calibrated and validated biochemical model forms the basis for the metabolic-isotopic coupling. As ΔG_{net} becomes increasingly negative (e.g., with increasing [H_2]), the individual reactions in the pathway depart from equilibrium to various extents (Fig. 2). We quantify the departure from equilibrium of individual reaction i by the reaction reversibility, defined as the ratio of the reverse to forward gross rates of that reaction and related to its actual Gibbs free energy ($\Delta G_{r,i}$) (26, 37, 38):

$$J_i^- / J_i^+ = \exp(\Delta G_{r,i}/RT) \ , \tag{2}$$

where R is the gas constant (J mol^{-1} K^{-1}), T is the temperature (K) and $\Delta G_{r,i} = \Delta G'^0_{r,i} + RT \ln Q$ (J mol^{-1}, where Q is the reaction quotient). We henceforth omit the subscripted i from the individual reaction $\Delta G'^0_r$ and ΔG_r.

For net forward methanogenesis rates, the reversibility (J_i^- / J_i^+) of individual reactions varies between zero (a near-unidirectional, kinetically controlled reaction) and unity (a near-equilibrium reaction). The uncertainty in reaction reversibility (gray envelopes in Fig. 2) is due to the unknown K_M values, which are drawn from distributions produced in the metabolic model calibration pro-

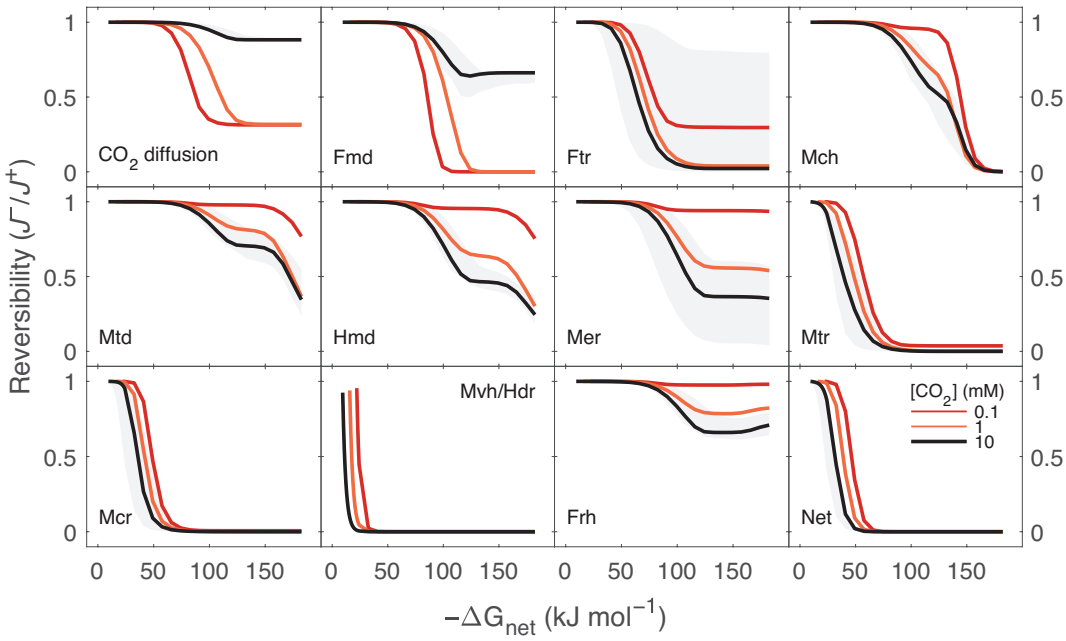

Figure 2: Reversibility of reactions in hydrogenotrophic methanogenesis. Reaction reversibility (J_i^-/J_i^+) against ΔG_{net}. The short names of the enzymes are in accordance with Fig. 1A and table S1. The 'Net' reversibility shown in the lower right panel is the CO_2-CH_4 reversibility, which is determined as the product of the individual reversibilities of the reactions in the carbon pathway (Fmd to Mcr). The median (black line) and 68% (gray envelope) of 10^3 model simulations with 10 mM [CO_2] are shown. The envelope represents K_M values that were drawn from posterior distributions resulting from the model calibration (see Methods, fig. S2 and table S5). The medians of simulations with [CO_2] of 0.1 and 1 mM are shown in red and orange lines, respectively. Simulations were carried out at [H_2] of 1 nM to 10 mM and [CH_4] of 10 μM.

cess (Methods, fig. S2). Some reactions do not become completely irreversible ($J_i^-/J_i^+ \to 0$) over the explored ΔG_{net} range (e.g., the Frh-catalyzed reduction of F_{420}), whereas others depart from a reversibility of unity at ΔG_{net} as modestly negative as -15 kJ mol^{-1} (Mvh/Hdr-catalyzed reaction) and -50 kJ mol^{-1} (Mcr and Mtr-catalyzed reactions) and become near-irreversible. We note that net methane production in our model is only possible at ΔG_{net} values more negative than ≈ -10 kJ mol^{-1}, a threshold below which ATP production is not possible (Methods). The differential response of the individual reaction reversibilities to changes in ΔG_{net} is a combined function of the reaction thermodynamics ($\Delta G_r'^0$) and the enzyme kinetics, specifically the V^+ and K_M values. Neither $\Delta G_r'^0$ nor V^+ and K_M in isolation predict the pattern of differential departure from equilibrium—coupled thermodynamics and kinetics must be considered.

An isotopic model calibrated to laboratory cultures

The isotopic discrimination between substrate (s) and product (p) is described by the isotopic fractionation factor ${}^{r}\alpha_{s/p} = {}^{r}\mathrm{R}_s/{}^{r}\mathrm{R}_p$, where ^{13}R = ^{13}C/^{12}C, ^{2}R = D/H (with D $\equiv$ ^{2}H and H $\equiv$ ^{1}H), and "r" denotes the rare isotope. The net isotopic fractionation expressed in an individual (bio)chemical reaction may vary between thermodynamic equilibrium and kinetic end-members, associated respectively with a reversible reaction and unidirectional forward reaction to form the reaction product. The equilibrium isotopic fractionation factor (EFF) between s and p is denoted by $\alpha^{\mathrm{eq}}_{s\text{-}p}$, and the kinetic fractionation factors (KFFs) are denoted by α^{+} or α^{-} for the forward and reverse direction of the reaction, respectively. The EFFs are related to the KFFs of the respective reaction by $\alpha^{\mathrm{eq}}_{s\text{-}p} = \alpha^{-}/\alpha^{+}$. Normal KFFs, where the isotopically heavy substrate reacts more slowly than the isotopically light substrate, are by definition smaller than unity. As most α values are close to unity, we use the ε notation for convenient comparison of fractionations ($\varepsilon = 1 - \alpha$, in parts per thousand, ‰).

With the forward and reverse gross fluxes calculated in the metabolic model and with values assigned to the EFFs and KFFs of the individual reactions, an isotopic mass balance may be solved for the net isotopic fractionation between the pathway substrates and products (25, 39). The uncertainty on calculated EFFs is relatively small (40), while most KFFs in hydrogenotrophic methanogenesis are unknown, and we drew their values from uniform distributions (Methods). Model $\Delta\mathrm{G}_{\mathrm{net}}$–fractionation relations calculated with the randomly drawn KFF values were compared to experimental data, and were used to generate distributions of the KFF values that minimize model-measurement mismatch (Methods, fig. S3). The ranges of KFF values calibrated in this way are the main source of uncertainty in the isotopic model (i.e., main reason for the uncertainty envelopes in Fig. 3). We note that existing CH_4–H_2O hydrogen isotope fractionations from culture experiments conducted under similar conditions differ by as much as ≈100‰ at a given $\Delta\mathrm{G}_{\mathrm{net}}$ value (e.g., 20, 41, fig. S4). We calibrated the hydrogen isotope KFFs against a curated dataset, which includes only a subset of the experimental data (Supplementary Materials, SM), and tested the effects of this choice on the posterior KFF distributions. We found relative insensitivity to the choice

of calibration dataset, other than for the KFF of Mvh/Hdr, which has smaller (i.e., less-negative) best-fit values when the calibration includes all of the experimental data (fig. S5) instead of the curated dataset. All other inferences made on the basis of the calibrated model are robust to the choice of calibration dataset.

After calibration of the carbon and hydrogen isotope KFFs to experimental data, we used the model (with no further tuning of the isotopic parameters) to determine the relations between ΔG_{net} and the abundances of doubly substituted ("clumped") methane isotopologues, which have yet to be systematically explored in experiments.

Bulk carbon isotope fractionation between CO_2 and CH_4

In laboratory cultures, the CO_2–CH_4 carbon isotope fractionation ($^{13}\varepsilon_{CO_2\text{-}CH_4}$) is inversely related to ΔG_{net} (16–21, fig. S4A). At near-zero ΔG_{net}, the individual reactions in the pathway operate close to equilibrium ($J_i^-/J_i^+ \to 1$), and our model predicts $^{13}\varepsilon_{CO_2\text{-}CH_4}$ close to the temperature-dependent isotopic equilibrium fractionation ($^{13}\varepsilon^{eq}_{CO_2\text{-}CH_4}$). When ΔG_{net} becomes slightly negative, $^{13}\varepsilon_{CO_2\text{-}CH_4}$ peaks to larger-than-equilibrium values of 80–100‰ at ΔG_{net} of ≈ -45 kJ mol^{-1}, followed by a gradual decline to ≈30‰ reached at ΔG_{net} of ≈ -120 kJ mol^{-1} (Fig. 3A,B). Such larger-than-equilibrium $^{13}\varepsilon_{CO_2\text{-}CH_4}$ values have been observed in several experimental and environmental datasets, and have been suggested to reflect a switch from an equilibrium to a kinetic fractionation in one of the network steps, with a KFF that is larger than the EFF (42). Our model reveals that this ΔG_{net}–$^{13}\varepsilon_{CO_2\text{-}CH_4}$ relation is indeed controlled by the landscape of combined departure from equilibrium of several reactions in the pathway. The carbon reaction network in methanogenesis is linear. In such networks, near-unidirectionality of an individual reaction ($J_i^-/J_i^+ \to 0$) leads to expression of that reaction's KFF and suppresses isotopic fractionation associated with downstream reactions (25). The Mcr-and Mtr-catalyzed reactions depart from equilibrium simultaneously at ΔG_{net} of ≈ -25 kJ mol^{-1}, and our model identifies the peak in $^{13}\varepsilon_{CO_2\text{-}CH_4}$ to reflect a weighted sum of these specific enzymes' KFFs and the sum of EFFs of the upstream reactions (Fig. 2). The experimentally measured KFF of Mcr (−38‰, Ref. 43) is larger than its EFF (1‰, Ref. 44), and so

is the model predicted KFF of Mtr ($\approx -28‰$) relative to its EFF (15‰, Ref. 44). Hence, partial expression of these KFFs results in the larger-than-equilibrium ${}^{13}\varepsilon_{CO_2\text{-}CH_4}$ at modestly negative ΔG_{net} values. The ${}^{13}\varepsilon_{CO_2\text{-}CH_4}$ floor at ΔG_{net} more negative than ≈ -120 kJ mol^{-1} (Fig. 3A,B) is defined by partial expression of the KFFs of Ftr and Fmd, and suppression of the isotopic fractionations associated with downstream reactions.

At large-negative ΔG_{net} values ${}^{13}\varepsilon_{CO_2\text{-}CH_4}$ is sensitive also to the extracellular partial pressure of CO_2 (pCO_2). At a steady state, intracellular CO_2 utilization is exactly matched by net CO_2 diffusion across the membrane. This net diffusive flux is the difference between large gross fluxes (into and out of the cell) when pCO_2 is high, and smaller gross fluxes at lower pCO_2. Thus, the reversibility of net diffusion is low at low pCO_2 ($J_i^- / J_i^+ \to 0$), and suppression of downstream net carbon isotopic fractionation results in small ${}^{13}\varepsilon_{CO_2\text{-}CH_4}$ (also referred to as a "reservoir effect"). The dependence of ${}^{13}\varepsilon_{CO_2\text{-}CH_4}$ on pCO_2 explains the smallest net fractionations observed in laboratory cultures (Fig. 3C, Ref. 18), as well as the dependence of ${}^{13}\varepsilon_{CO_2\text{-}CH_4}$ on pH in hyperalkaline settings (45, 46).

Carbon isotope fractionation between CO_2 and a biomass precursor

We compared the results of the calibrated metabolic-isotopic model to measurements of the CO_2–biomass carbon isotope fractionation. About a third of the carbon in the biomass of hydrogenotrophic methanogens derives from CH_3-H_4MPT produced in the methanogenesis pathway, $\sim$5% of which is directed to biomass production in laboratory cultures of methanogens that have no membrane-associated methanophenazines (47). In natural environments, and especially under energy limitation, the fraction of CH_3-H_4MPT directed to form biomass may be substantially smaller. Hence, we assumed that this biomass shunt has only a minor effect on the net CO_2–CH_4 carbon isotope fractionation and did not explicitly include it in our model. Another third (approximately) of the biomass carbon derives from reduction of CO_2 to CO and the subsequent condensation of a carbonyl moiety with the CH_3-H_4MPT-derived methyl moiety to form acetyl coenzyme A (acetyl-CoA, Ref. 48). The last third (approximately) of the carbon in hydrogenotrophic methanogen

biomass comes from various carboxylation reactions (49).

Within the above framework, the carbon isotope composition of biomass can be expressed as a function of the isotopic compositions of CO_2 and CH_3-H_4MPT, and a composite isotopic fractionation, which represents an appropriately weighted combination of the fractionations associated with the various biosynthesis reactions (Eq. S3, SM). The model carbon isotope fractionation between CO_2 and CH_3-H_4MPT ($^{13}\varepsilon_{CO_2\text{-}CH_3}$) covaries with $^{13}\varepsilon_{CO_2\text{-}CH_4}$ with a slope of ≈0.95 (fig. S6). With a few exceptions, observed carbon isotope fractionations between CO_2 and biomass ($^{13}\varepsilon_{CO_2\text{-}B}$, Refs. 50–52) covary with $^{13}\varepsilon_{CO_2\text{-}CH_4}$ along a scattered array with a slightly shallower slope (≈0.73, R^2 = 0.72), which is offset from the model $^{13}\varepsilon_{CO_2\text{-}CH_3}$–$^{13}\varepsilon_{CO_2\text{-}CH_4}$ curve by ≈10–30‰ (fig. S6). Isotopic mass balance requires that to maintain this approximately constant offset (≈20±10‰) between the $^{13}\varepsilon_{CO_2\text{-}CH_3}$–$^{13}\varepsilon_{CO_2\text{-}CH_4}$ curve and the observed $^{13}\varepsilon_{CO_2\text{-}B}$–$^{13}\varepsilon_{CO_2\text{-}CH_4}$ array, the composite carbon isotope fractionation associated with biosynthesis reactions (e.g., CO_2 reduction, acetyl-CoA condensation, carboxylation) must covary with $^{13}\varepsilon_{CO_2\text{-}CH_4}$ (Eq. S3, SM). In other words, with increasingly negative ΔG_{net}, as $^{13}\varepsilon_{CO_2\text{-}CH_4}$ departs from CO_2–CH_4 carbon isotope equilibrium and gradually decreases towards the KFFs of Ftr and Fmd, so does the composite biosynthesis fractionation depart from isotopic equilibrium towards a kinetically-controlled fractionation. This implies back reaction in at least some of the biosynthesis reactions, though we cannot confidently identify which reactions.

Bulk hydrogen isotope fractionation between CH_4 and H_2O

In the case of hydrogen isotopes, we express the CH_4–H_2O fractionation ($^{2}\varepsilon_{CH_4\text{-}H_2O}$) rather than the H_2O–CH_4 fractionation, which is opposite in sign. This choice maintains a common sense of departure from equilibrium, in which both $^{13}\varepsilon_{CO_2\text{-}CH_4}$ and $^{2}\varepsilon_{CH_4\text{-}H_2O}$ values decrease with increasingly negative ΔG_{net}. In laboratory cultures, $^{2}\varepsilon_{CH_4\text{-}H_2O}$ is ≈200‰ more negative than the temperature-dependent isotopic equilibrium fractionation ($^{2}\varepsilon^{eq}_{CH_4\text{-}H_2O}$), and existing observations suggest that it does not display a clear dependence on ΔG_{net} (16, 19, 20, 41, 53, fig. S4B). Unlike the linear carbon reaction network, the hydrogen reaction network has four branches, each of which has the potential

for hydrogen atom exchange between pathway intermediates and H_2O. Therefore, departure from equilibrium of one of the hydrogen atom exchange reactions does not preclude CH_4-H_2O hydrogen isotopic equilibrium. Specifically, the Mvh/Hdr-catalyzed reaction is near-irreversible at ΔG_{net} values as high as -25 kJ mol^{-1} (Fig. 2), yet at this ΔG_{net} value ${}^2\varepsilon_{CH_4\text{-}H_2O}$ is approximately equal to ${}^2\varepsilon^{eq}_{CH_4\text{-}H_2O}$ (Fig. 3D, E), and this arises from the high reversibility of the other hydrogen atom exchange reactions in the pathway. Only when the Mcr- and Mtr-catalyzed reactions sufficiently depart from reversibility (at $\Delta G_{net} \leq -30$ kJ mol^{-1}), cutting off methane and HS-CoB from exchange with upstream intermediates that are close to hydrogen isotope equilibrium with H_2O, does ${}^2\varepsilon_{CH_4\text{-}H_2O}$ depart from ${}^2\varepsilon^{eq}_{CH_4\text{-}H_2O}$ (Fig. 3D, E). At ΔG_{net} more negative than -40 kJ mol^{-1} the KFFs of Mcr, Mtr and Mvh/Hdr control ${}^2\varepsilon_{CH_4\text{-}H_2O}$ (fig. S3). In addition to explaining the mechanism of departure from hydrogen isotope equilibrium, our model predicts a clear ${}^2\varepsilon_{CH_4\text{-}H_2O}$–$\Delta G_{net}$ relation, which has not been accessed by the range of ΔG_{net} explored in laboratory cultures to date.

The hydrogen atom added to CH-H_4MPT may come from F_{420} (which exchanges hydrogen atoms with H_2O) in the Mtd-catalyzed reaction, or from H_2 in the Hmd-catalyzed reaction (54, Fig. 1A). Thus, up to one quarter of the hydrogen atoms in methane may come directly from H_2, depending on the relative activity of Mtd and Hmd. Intracellular H_2 rapidly exchanges hydrogen atoms with H_2O due to the activity of various hydrogenases, and this exchange results in isotopic equilibrium (55, 56) in which H_2 is strongly depleted in deuterium relative to H_2O ($\alpha^{eq}_{H_2O\text{-}H_2}$ of $\approx$3 at 60°C, Ref. 57). High growth rates at high H_2 concentrations favor Hmd activity over Mtd (35, 54). Under these conditions, even though the H_2 may itself be in hydrogen isotope equilibrium with the H_2O, kinetically-controlled incorporation of hydrogen isotopes directly from D-depleted H_2 may result in disequilibrium ${}^2\varepsilon_{CH_4\text{-}H_2O}$ (Fig. 3D, E). In some cases, which probably only occur under extreme experimental conditions such as isotopic labeling, intracellular H_2O–H_2 isotopic disequilibrium may exist. If Hmd is active in such conditions, ${}^2\varepsilon_{CH_4\text{-}H_2O}$ may vary in response to variations in the hydrogen isotope composition of H_2. Our model captures this behavior, as observed in a rapidly growing methanogenic culture at 60°C (20), which displayed ${}^2\varepsilon_{CH_4\text{-}H_2O}$ values between -145‰ and -480‰ that covary with the H_2O-H_2 hydrogen isotope fractionation

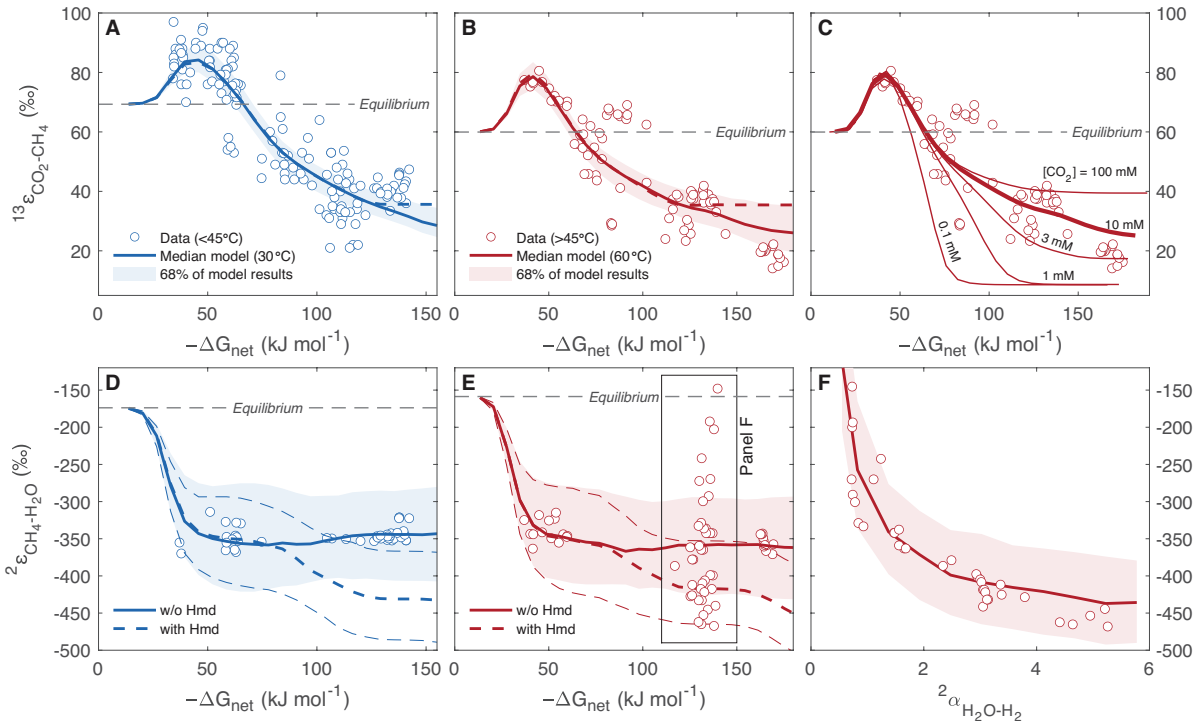

Figure 3: Model-laboratory culture comparison of bulk carbon and hydrogen isotope fractionation. Mesophilic (30–40°C, blue circles) and thermophilic (≥55°C, red circles) experimental data and model results (lines and envelopes) at 30°C (blue) and 60°C (red), and the equilibrium isotopic fractionation (dashed lines). (**A-B, D-E**) $^{13}\varepsilon_{CO_2\text{-}CH_4}$ and $^{2}\varepsilon_{CH_4\text{-}H_2O}$ against ΔG_{net}. The envelopes represent 68% of 10^3 model simulations, with KFFs drawn from calibrated distributions (see Methods and fig. S3). (**C**) $^{13}\varepsilon_{CO_2\text{-}CH_4}$ against ΔG_{net} for different extracellular CO_2 concentrations ($[CO_2]$, shown next to the corresponding model curve). (**F**) Mixing effects on $^{2}\varepsilon_{CH_4\text{-}H_2O}$ as a function of the H_2O–H_2 isotopic fractionation ($^{2}\alpha_{H_2O\text{-}H_2}$), compared to laboratory culture data at 60°C (20). The envelope represents 68% of 10^3 model simulations, with KFFs drawn from calibrated distributions.

(Fig. 3F).

Clumped isotopologue distributions

The abundances of the doubly substituted isotopologues of methane ($^{13}CH_3D$ and $^{12}CH_2D_2$) are expressed as a deviation from their concentrations at a stochastic distribution of the rare isotopes, with $\Delta^{13}CH_3D = {}^{13CH_3D}R_{sample}/{}^{13CH_3D}R_{stochastic} - 1$ [‰], and $\Delta^{12}CH_2D_2 = {}^{12CH_2D_2}R_{sample}/{}^{12CH_2D_2}R_{stochastic} - 1$ [‰]. Both $\Delta^{13}CH_3D$ and $\Delta^{12}CH_2D_2$ values depend on the methane formation temperature (58), yet applications of methane clumped isotopes to constrain its formation temperature and mechanism are complicated by source mixing and disequilibrium effects (23, 59). The dependence of

$\Delta^{13}CH_3D$ and $\Delta^{12}CH_2D_2$ on ΔG_{net} has not been determined experimentally, and our full metabolic-isotopic model predicts that departure from clumped isotope equilibrium is non-monotonic (Fig. 4 and fig. S7), in contrast with previous estimates of these relations that were based on simpler models (22, 23). As ΔG_{net} becomes negative, both $\Delta^{13}CH_3D$ and $\Delta^{12}CH_2D_2$ values decrease from the expected equilibrium compositions, and $\Delta^{12}CH_2D_2$ becomes anti-clumped (i.e., $< 0‰$) due to expression of the KFFs of the Mcr- and Mtr-catalyzed reactions (fig. S7). After the initial decrease in $\Delta^{13}CH_3D$ and $\Delta^{12}CH_2D_2$, both increase with increasingly negative ΔG_{net}, and $\Delta^{13}CH_3D$ increases to values almost as high as the equilibrium values (Fig. 4A). This behavior has two implications. First, there is a range of ΔG_{net} (≈ -70 to -90 kJ mol^{-1}) over which $\Delta^{13}CH_3D$ values may give the false appearance of proximity to isotopic equilibrium. Second, there is a range of ΔG_{net} (≈ -80 to -30 kJ mol^{-1}) over which $\Delta^{13}CH_3D$ and $\Delta^{12}CH_2D_2$ cannot uniquely constrain the energetic state of the cell (e.g., $\Delta^{13}CH_3D$ is ≈ 4 ‰ at both ΔG_{net} of ≈ -25 and ≈ -80 kJ mol^{-1}). However, in combination with ${}^{13}\varepsilon_{CO_2\text{-}CH_4}$ and ${}^{2}\varepsilon_{CH_4\text{-}H_2O}$ data, the position in the ΔG_{net} landscape and the degree of departure from equilibrium may be uniquely constrained (Fig. 4B,C). The multiple-isotope composition of methane (i.e., bulk carbon and hydrogen, and clumped isotopes), interpreted within the quantitative framework provided by our metabolic-isotopic model, may thus be a useful proxy for ΔG_{net} in environments where measurements of H_2, CO_2 and CH_4 concentrations in the cells' immediate vicinity are not easily obtainable. In addition to departure from equilibrium of the Mcr- and Mtr-catalyzed reactions, which may cause anti-clumped $\Delta^{12}CH_2D_2$ compositions, another testable prediction of our model is that the Hmd-catalyzed reaction may also cause anti-clumping. This arises from combinatorial effects, which are caused by mixing of hydrogen atom sources with a different hydrogen isotope composition (δD) and are proportional to the difference in δD values between the sources (60–62). The combinatorial effects are expected to be most clearly expressed in conditions that promote H_2O-H_2 hydrogen isotope disequilibrium, such as isotope labeling experiments (fig. S8).

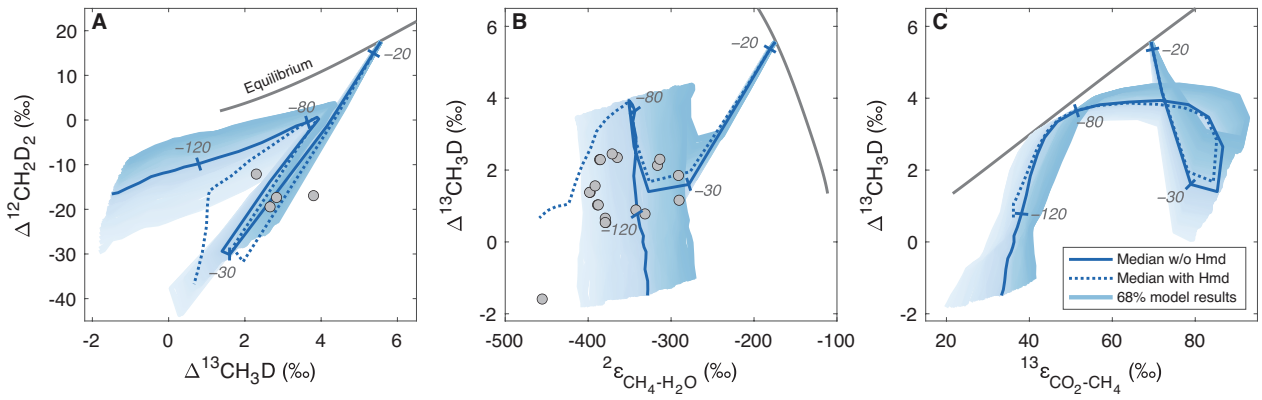

Figure 4: Model-laboratory culture comparison of clumped isotopologue abundances. Experimental data (gray circles) and model results (lines and envelopes) of 200 simulations at 30°C. The dark gray lines represent temperature-dependent isotopic equilibrium at 0-350°C, and the thick blue lines show the median of the simulations, with tick marks at ΔG_{net} values of -20, -30, -80, and -120 kJ mol^{-1}. The envelopes represent 68% of 200 model simulations, with KFFs drawn from calibrated distributions. (**A**) $\Delta^{13}CH_3D$ against $\Delta^{12}CH_2D_2$. (**B**) $\Delta^{13}CH_3D$ against ${}^{2}\varepsilon_{CH_4\text{-}H_2O}$. (**C**) $\Delta^{13}CH_3D$ against ${}^{13}\varepsilon_{CO_2\text{-}CH_4}$. Laboratory culture samples are from hydrogenotrophic methanogens that do not have membrane-associated methanophenazines. The model results under thermophilic conditions are in fig. S9.

Apparent *vs.* actual isotopic equilibrium in laboratory cultures

Our predicted trajectories for departure from equilibrium ${}^{13}\varepsilon_{CO_2\text{-}CH_4}$, ${}^{2}\varepsilon_{CH_4\text{-}H_2O}$, $\Delta^{13}CH_3D$ and $\Delta^{12}CH_2D_2$ values and comparison to available data suggest that to date, carbon, hydrogen and clumped isotope equilibrium has not been obtained in methanogenic laboratory cultures. This is not entirely surprising, as biological activity is by definition out of equilibrium. However, if ΔG_{net} is small enough, isotopic fractionations can be practically indistinguishable from true isotopic equilibrium. In several experiments, near-equilibrium ${}^{13}\varepsilon_{CO_2\text{-}CH_4}$ values co-occur with clearly disequilibrium ${}^{2}\varepsilon_{CH_4\text{-}H_2O}$ values, which have been previously explained by a decoupling of the carbon and hydrogen isotope systems in methanogenesis (20, 63). Based on the results of our mechanistic metabolic-isotopic model, we suggest instead that the measured near-equilibrium ${}^{13}\varepsilon_{CO_2\text{-}CH_4}$ values did not reflect isotopic equilibrium, but the descending branch from the ${}^{13}\varepsilon_{CO_2\text{-}CH_4}$ maximum (which occurs at $\Delta G_{net} \approx -40$ kJ mol^{-1}) with increasingly negative ΔG_{net}. In other words, we suggest that apparent equilibrium ${}^{13}\varepsilon_{CO_2\text{-}CH_4}$ values may emerge by a fortuitous combination of EFFs and KFFs, and not due to actual isotopic equilibrium between CO_2 and methane. We further

suggest that experiments aimed at constraining isotopic equilibrium should be conducted at ΔG_{net} values that are not more negative than -20 kJ mol^{-1}. At more negative values, expression of KFFs will result in disequilibrium isotopic fractionations. Our model links ΔG_{net} values to the specific rates of methanogenesis (Fig. 1 and fig. S10), which are sometimes easier (than ΔG_{net}) to quantify in laboratory cultures and natural environments. Thus, our model may serve to plan future experiments in which the rate of methanogenesis is slow enough for sufficient isotopic exchange between methane, CO_2 and H_2O to achieve near-equilibrium isotopic distributions and internal equilibration of the clumped isotopologues.

Isotopic fractionation in energy-limited environments

The metabolic-isotopic model may be used to examine the controls on the isotopic fractionation of methanogenesis not only in laboratory cultures, but in natural environments as well. Laboratory cultures operate far from equilibrium, usually at [H_2] and cell-specific methanogenesis rates (csMR) much higher than those in natural environments (table S6; fig. S10). Recent reevaluations of slowly forming biogenic methane sources such as marine sediments, coalbeds or shale gas deposits, revealed that apparent CH_4–CO_2 and CH_4–H_2O isotopic equilibrium is common (20, 42, 44, 64–66). We used our model to study the isotopic effects in such settings, by adopting enzyme kinetic parameters obtained from methanogens grown under energy limitation. Such conditions promote the activity of the Mcr I isoenzyme at the expense of the Mcr II isoenzyme (35, 36, Methods). We used the modified model to calculate the csMR and isotopic effects at 0-60°C, and assessed the resulting ΔG_{net}–csMR–isotopic relations.

Existing estimates of environmental ΔG_{net} of hydrogenotrophic methanogenesis are more positive than -30 kJ mol^{-1} (table S6). However, the determination of ΔG_{net} in natural environments is often difficult because of low and spatially heterogeneous in-situ [H_2] (67–69), and the actual range of ΔG_{net} likely reflects this heterogeneity. As ΔG_{net} determines the csMR (fig. S10), which is easier to measure, we henceforth discuss csMR–isotopic fractionation relations. Our model predictions of csMR in energy-limited environments (10^{-5} to 1 fmol cell^{-1} d^{-1}) are considerably lower

than the typical range in laboratory cultures (10 to 10^4 fmol cell^{-1} d^{-1}, fig. S10, Refs. 21, 53). This csMR difference of several orders of magnitude reflects the model calibration to reproduce [H_2]–csMR relations in low-[H_2] laboratory culture experiments (Fig. 1B). Although this calibration was limited to available experimental [H_2] higher than 1 μM, our predicted csMR values at $\sim$nM H_2 concentrations (10^{-5} to 1 fmol cell^{-1} d^{-1}) overlap with the range of csMR values from shallow and deep marine sediments (10^{-4} to 1 fmol cell^{-1} d^{-1}), which we calculated from reported bulk methanogenesis rates and cell densities (table S7). We note that there is large uncertainty regarding these environmental csMR values, which stems in part from uncertainty on the net rate of methanogenesis. The methanogenesis rate in natural environments is often determined by radiotracer assays, which may lead to an overestimation of the net methanogenesis rate by orders of magnitude if the reversibility of net methanogenesis (i.e., between CO_2 and methane) is higher than 0.9 (Fig. 2). An additional source of uncertainty is the number of active methanogenic cells in the sediments, and there are currently very limited estimates of these values. Despite these uncertainties, our model predictions of csMR match not only environmental csMR estimates, but also estimates of cell-specific power utilization, $P = -\Delta G_{net} \times$ csMR [W cell^{-1}]. We predict P between 10^{-22} and 10^{-18} W cell^{-1} for ΔG_{net} between -10 to -30 kJ mol^{-1} respectively, at 10°C, in agreement with previously estimated cell-specific power utilization in marine sediments (70).

The model reveals that in contrast to methanogenesis in lab cultures, under energy-limited conditions the Mtr-catalyzed reaction departs from equilibrium before the Mcr-catalyzed reaction (fig. S11). As a consequence, different csMR–fractionation relations emerge, most notably an initially attenuated response of ${}^{13}\varepsilon_{CO_2\text{-}CH_4}$ values to increasing csMR (Fig. 5A). Specifically, ${}^{13}\varepsilon_{CO_2\text{-}CH_4}$ displays a much more muted increase to larger-than-equilibrium values with increasing csMR in the low-energy-calibrated model than in the high-energy-calibrated model. The reason for this apparent carbon isotopic equilibrium is the smaller magnitude of the KFF of Mtr relative to Mcr (-29‰ and -38‰ at 60°C, respectively, fig. S3). Thus, as the Mtr-catalyzed reaction departs from equilibrium, the net carbon isotope fractionation remains within $\approx$5‰ of ${}^{13}\varepsilon^{eq}_{CO_2\text{-}CH_4}$ up to a csMR of $\sim$10 fmol cell^{-1} d^{-1} (Fig. 5). An environmental prediction of the above is that ${}^{13}\varepsilon_{CO_2\text{-}CH_4}$

that differs measurably from $^{13}\varepsilon^{eq}_{CO_2\text{-}CH_4}$ indicates csMR higher than $\sim$10 fmol cell^{-1} d^{-1}.

Analytically distinguishable departure of $^{2}\varepsilon_{CH_4\text{-}H_2O}$ from equilibrium occurs at csMR between $\sim$0.001 and 0.1 fmol cell^{-1} d^{-1} (at 0°C and 60°C, respectively; fig. S12B), and departure from clumped isotope equilibrium occurs over a similar range of csMR (fig. S12C, D). If hydrogenotrophic methanogens can be cultured at such low csMR (small negative ΔG_{net}), an implication of the model csMR–isotopic fractionation relations is that experimental studies aimed at measuring methane that is close to bulk hydrogen isotope equilibrium would accumulate enough methane for analysis within a few days. In contrast, given existing analytical capabilities, accumulation of enough methane for clumped isotope analysis at csMR low enough to achieve isotopic near-equilibrium requires combinations of long experimental duration (hundreds of days) and large culture volume (hundreds of milliliters).

In addition to its utility for the design of culture experiments, our model predicts that at csMR between 0.1 and 10 fmol cell^{-1} d^{-1}, one should expect near-equilibrium $^{13}\varepsilon_{CO_2\text{-}CH_4}$ concurrent with disequilibrium $^{2}\varepsilon_{CH_4\text{-}H_2O}$. The opposite situation (i.e., near-equilibrium $^{2}\varepsilon_{CH_4\text{-}H_2O}$ and disequilibrium $^{13}\varepsilon_{CO_2\text{-}CH_4}$) is common in natural environments, though csMR is usually unknown. As suggested in previous studies, this apparent hydrogen isotope equilibrium concurrent with carbon isotope disequilibrium may be explained by diffusive mixing of CO_2 and/or methane from different depths within the sediment, or isotopic (Rayleigh) distillation (Fig. 5B; 42, 71, 72). Rayleigh distillation is not expected to be relevant for H_2O as its pool is large enough so that its composition will not change under environmentally plausible conditions. This is not the case for the much smaller dissolved inorganic carbon (DIC) pool, which can evolve isotopically upon progressive consumption. If disequilibrium $^{13}\varepsilon_{CO_2\text{-}CH_4}$ is explained as above (transport and/or Rayleigh distillation) rather than by microbial expression of KFFs, then the scarcity of data within the field representing disequilibrium microbial fractionation in Fig. 5B may reflect near-equilibrium isotopic fractionation during methanogenesis in energy-limited environments. An alternative explanation, that methane originally forms in both $^{13}\varepsilon_{CO_2\text{-}CH_4}$ and $^{2}\varepsilon_{CH_4\text{-}H_2O}$ disequilibrium (e.g., csMR>10 fmol cell^{-1} d^{-1} according to our model, Fig. 5A) and that subsequent enzymatically-catalyzed

hydrogen isotope exchange promotes ${}^{2}\varepsilon_{CH_4\text{-}H_2O}$ equilibrium (20), may not be consistent with the landscape of departure from equilibrium of the individual reactions predicted by our model. In this alternative explanation, diffusion of methane in and out of the cells and enzymatically-catalyzed hydrogen isotope exchange in the last steps of the methanogenesis pathway (the Mcr- and Hdr-catalyzed reactions) without net methane production, and possibly much later than the timing of methane formation, is suggested to lead to ${}^{2}\varepsilon_{CH_4\text{-}H_2O}$ equilibrium, while disequilibrium upstream of these reactions sustains ${}^{13}\varepsilon_{CO_2\text{-}CH_4}$ disequilibrium. However, we note that the Mcr- and Hdr-catalyzed reactions are the first to depart from equilibrium (Fig. 1, fig. S11). Our model reveals that near-equilibrium for these reactions, which is required to approach CH_4–H_2O hydrogen isotope equilibrium, implies near-equilibrium in the entire methanogenesis pathway. In this case, carbon isotope equilibration is also expected, contrary to the observations, suggesting that post-formation hydrogen isotope equilibration is not the cause for apparent equilibrium ${}^{2}\varepsilon_{CH_4\text{-}H_2O}$.

If, as argued above, apparent equilibrium ${}^{2}\varepsilon_{CH_4\text{-}H_2O}$ in natural environments is the outcome of near-equilibrium isotopic fractionation during methanogenesis, and not disequilibrium microbial frationation followed by Mcr- and Hdr-catalyzed equilibration of hydrogen isotopes, then implied csMR is lower than $\sim$0.001–0.1 fmol cell^{-1} d^{-1} (depending on temperature). This predicted range of csMR is consistent with almost all csMR estimated from cell abundances and volumetric methanogenesis rates (SM, table S7). In environments that support higher csMR and disequilibrium microbial fractionation, near-equilibrium ${}^{2}\varepsilon_{CH_4\text{-}H_2O}$ concurrent with disequilibrium ${}^{13}\varepsilon_{CO_2\text{-}CH_4}$ may instead be explained by methane cycling or anaerobic oxidation of methane that operates close to the thermodynamic limit of this metabolism (73). Alternatively, energy- and substrate-limited methanogenesis from methylated substrates (e.g., acetate, methanol) is expected to generate methane with more positive δ^{13}C values (74), and accordingly, smaller ${}^{13}\varepsilon_{CO_2\text{-}CH_4}$ values that depart from CO_2–CH_4 carbon isotope equilibrium.

By accounting for the metabolites and reactions in the hydrogenotrophic methanogenesis pathway, we link environmental substrate and product concentrations, pH and temperature to the energetics and net rate of methanogenesis, and to the associated fractionation of carbon, hydrogen

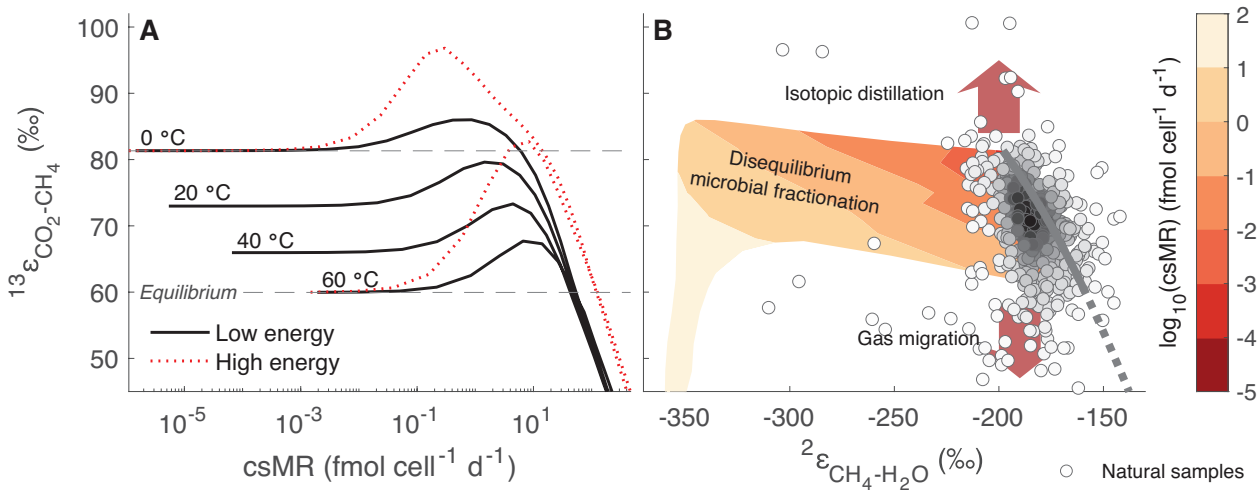

Figure 5: Isotopic fractionation during methanogenesis in energy-limited conditions. (**A**) $^{13}\varepsilon_{CO_2\text{-}CH_4}$ against cell-specific methanogenesis rate (csMR). Dotted red lines show the laboratory-calibrated model (high-energy) results at 0°C and 60°C. (**B**) $^{13}\varepsilon_{CO_2\text{-}CH_4}$ against $^{2}\varepsilon_{CH_4\text{-}H_2O}$. Contours are $\log_{10}$(csMR) predicted by our model, between 0°C and 60°C. The calculations are for [H_2] between 1 nM and 5 μM, [CO_2] and [CH_4] of 1 mM, and a cell volume of 1 μm^3. The circles are biogenic environmental samples from marine sediments, coalbed methane and natural gas deposits (n = 491), colored by the frequency of occurrence, and showing that most samples plot close to the isotopic equilibrium curve.

and clumped isotopes. The landscape of departure of individual reactions in the pathway from reversibility controls these fractionations, mechanistically explaining rate–fractionation relations in laboratory cultures. We suggest that a combination of $^{13}\varepsilon_{CO_2\text{-}CH_4}$, $^{2}\varepsilon_{CH_4\text{-}H_2O}$, $\Delta^{13}CH_3D$ and $\Delta^{12}CH_2D_2$ data, interpreted within a metabolic-isotopic model framework, can uniquely constrain the in-situ energetics of methanogenic activity (i.e., the actual ΔG_{net} of methanogenesis), which may be difficult to constrain by other means. However, application of such an approach is limited to natural and artificial environments in which hydrogenotrophic methane production is the dominant control over the apparent CH_4–CO_2 and CH_4–H_2O isotopic fractionations, and where other processes are less important. Such processes include CO_2 and methane diffusion, isotopic distillation and methane cycling, which are prevalent in natural environments. Nevertheless, the mechanistic understanding of isotopic effects during microbial methanogenesis provided by our model allows an inference that this metabolism operates close to chemical and isotopic equilibrium in a wide range of natural environments, including marine sediments, coal beds and natural gas

deposits.

Methods

Relating net isotopic fractionation to thermodynamic drive

The metabolic-isotopic model that we developed is based on a general framework, previously used to investigate sulfur isotopes in microbial sulfate-reduction (25, 39). This approach is applicable to any metabolic network with some modifications that we present below. In general, the net flux of a reversible enzymatically catalyzed reaction (J) is defined by the difference between the forward (J^+) and backward (J^-) gross fluxes, and can be expressed as (26):

$$J = J^+ - J^- = V^+ \times \left(\frac{\prod_j \left(\left[r_j \right] / K_{M_j} \right)^{n_j}}{1 + \prod_j \left(\left[r_j \right] / K_{M_j} \right)^{n_j} + \prod_i \left(\left[p_i \right] / K_{M_i} \right)^{m_i}} \right) \times \left(1 - e^{\Delta G_i / RT} \right) , \qquad (3)$$

where V^+ is the maximal rate capacity of the enzyme (defined by $[\mathrm{E}] \times k^+_{cat}$, where k^+_{cat} is the catalytic rate constant for forward reaction and [E] is the enzyme concentration), $[r_j]$ and $[p_i]$ are concentrations of the ith reactant and jth product, respectively, and K_{M_j} and K_{M_i} are the Michaelis constants for the forward and reverse directions, respectively. The n_j and m_i stand for the stoichiometry of the reactant and product, respectively. A net flux, as described by Eq. 3, is calculated for each of the reactions in the hydrogenotrophic methanogenesis pathway (table S1). These fluxes are used to construct a mass balance, which is solved at a steady-state to find the concentrations of the metabolites. The steady-state solution was obtained by forward integration using ode15s, an ordinary differential equation (ODE) solver in MATLAB®. Metabolite concentrations in the model span 6 to 7 orders of magnitude, but all are linked by identical net rates, and this results in orders of magnitude differences among the residence times of the different metabolites. The set of ODEs is thus 'stiff', requiring a solution algorithm that would prevent unreasonably small time steps, which could lead to long computation times or failure of the model. This problem thus required the use of the ode15s solver with an absolute tolerance of 10^{-20} M. We checked that the duration of integration was sufficient to reach a steady-state solution (i.e., no change in concentrations and fluxes) in all cases.

The model's inputs include the environmental temperature, pH and extracellular aqueous concentrations of H_2, CO_2 and CH_4. We assume that the intracellular concentrations of H_2 and CH_4 are equal to the extracellular concentrations due to their rapid diffusion through the membrane. For CO_2, we apply a simple diffusion model to relate intracellular to extracellular CO_2 concentrations. The model's tunable parameters include enzyme kinetic constants (K_M and V^+), thermodynamic constants ($\Delta G_r'^0$) and cellular parameters such as cell size, and concentrations of some of the metabolites. We elaborate on the parameters and the choice of their values below. With the inputs prescribed and values for the tunable parameters chosen, the model outputs are the concentrations of all intracellular metabolites and the gross fluxes among these metabolites, which are related to the reactions in the methanogenesis pathway.

We used the forward and backward gross fluxes from the metabolic model to calculate the net isotopic fractionations in hydrogenotrophic methanogenesis. To this end, we constructed a mass balance for each isotopic system (for both bulk and clumped isotopes), which is based on calculating an isotopic flux associated with each of the chemical fluxes. For the schematic reaction $r \rightarrow p$, this isotopic flux can be approximated:

$$F_{rp} = J_{rp}^{+} R_r \alpha_{rp,r} \ , \tag{4}$$

where J_{rp}^{+} is the forward chemical flux between metabolite pools r and p, R_r is the abundance ratio of heavy to light isotopes in pool r, and $\alpha_{rp,r}$ is the KFF of the reaction. A term similar to Eq. 4 was assigned to account for the consumption and production of each (singly- and doubly-substituted) isotopologue in the pathway while considering the stoichiometry and the symmetry coefficients, where relevant, in a similar manner to previous model derivations (23, 24). As described above, these terms were used to construct isotopic mass balances in the form of a set of coupled differential equations, which were solved numerically using the ode15s solver in MATLAB® to obtain the steady-state bulk and clumped isotopic composition of all intracellular metabolites, given bulk extracellular D/H and $^{13}C/^{12}C$ of H_2O and CO_2, respectively.

The net isotopic fractionation in linear metabolic networks such as the carbon reaction network in hydrogenotrophic methanogenesis can be solved analytically. For example, in the case of the

reaction $r \rightleftarrows p$, the net isotopic fractionation between the metabolite pools of r and p ($\alpha_{r,p}^{net}$) can be calculated by:

$$\alpha_{r,p}^{net} = \left(\alpha_{r,p}^{eq} - \alpha_{r,rp}\right) \times (J_{pr}^{-}/J_{rp}^{+}) + \alpha_{r,rp} \ , \tag{5}$$

where $\alpha_{r,p}^{eq}$ is the EFF between pools r and p, $\alpha_{r,rp}$ is 1/KFF of the forward reaction. A full derivation for this term is presented in a previous study (25). The reversibility J_{pr}^{-}/J_{rp}^{+} is directly related to $\Delta G'_{r,i}$ through the flux-force relationship (Eq. 2). Eq. 5 can be expanded recursively to describe the net isotopic fractionation in a linear reaction network of arbitrary length (25). Such a recursive expression has the advantage of a significantly reduced computational time compared to the numerical solution that is used for nonlinear reaction networks. We verified that this analytical solution yields identical results to the numerical solution for the net carbon isotopic fractionation. We note that the solution in Eq. 5 is irrelevant for branched networks, such as those describing methane hydrogen isotopes or clumped isotopologues, and that an analytical solution for the full ODE sets of these systems in not feasible. Hydrogen and clumped isotopes require the computationally heavier numerical simulations that are described above.

Metabolic model parameters

We tested the model for input [H_2] ranges of 10^{-9} to 10^{-2} M, [CO_2] ranges of 0.1 to 100 mM, and [CH_4] was held at 10^{-5} M. These ranges were chosen to include concentrations reported in various culture experiments and guided by a sensitivity analysis, which showed that the model is relatively insensitive to [CH_4] but that it is sensitive to [H_2] and [CO_2]. In the figures, we present the model results for [CO_2] of 10 mM, [CH_4] of 10 μM, and at 60°C, unless stated otherwise. We numerically solve for the steady-state concentrations of 16 metabolites in the hydrogenotrophic methanogenesis pathway of *Methanothermobacter thermoautotrophicus*. The initial concentrations of the total (i.e., reduced and oxidized) electron carriers (Fd, coenzyme B, F_{420}) and H_4MPT were compiled from experimentally determined concentrations, where available (table S8).

Extracellular and intracellular concentrations of CO_2, H_2 and CH_4

The model was designed to predict intracellular metabolite concentrations of the hydrogenotrophic methanogenesis pathway at a steady state, by prescribing temperature, and extracellular [H_2], [CO_2], and [CH_4]. These small, non-polar molecules diffuse rapidly through the cell membrane, and it is often assumed that their intracellular aqueous concentrations are in equilibrium with the headspace gas (related to the aqueous concentrations through Henry's Law constants; table S8). We adopt this assumption for CH_4, to which the model is relatively insensitive. However, we explore two cases in which concentrations of CO_2 and H_2 are not in equilibrium with the headspace: (*i*) CO_2 diffusion through the membrane may become limiting with increasing net methanogenesis flux (75). We model intracellular CO_2 concentrations ([$CO_{2(in)}$]) using Fick's Law:

$$J_{\mathrm{dif}} = D \times A \times \frac{[\mathrm{CO}_{2(\mathrm{out})}] - [\mathrm{CO}_{2(\mathrm{in})}]}{z} \,, \tag{6}$$

where J_{dif} is the net CO_2 diffusive flux, D is the permeability constant, A is the membrane surface area, z is the membrane width and [$CO_{2(out)}$] is the extracellular CO_2 concentration. To determine A we assume that the cells are spherical, and relate their volume (V_{cell}) to A via the cell's radius (r_{cell}) where:

$$r_{\mathrm{cell}} = \sqrt[3]{\frac{3}{4}\frac{V_{\mathrm{cell}}}{\pi}} \,, \tag{7}$$

and:

$$A = 4 \times \pi \times r_{\mathrm{cell}}^2 \,. \tag{8}$$

The values that we used for D, z and V_{cell} are listed in table S8. (*ii*) Cultivation of methanogens under low [H_2] conditions requires growth in co-cultures with H_2-producing (hydrogenic) bacteria (17, 20). Juxtaposition of methanogens and hydrogenic bacteria may result in immediate consumption of bacterially produced H_2 by the methanogens, which may result in spatially heterogeneous H_2 concentrations (67, 68). In this case, the aqueous H_2 concentration in the immediate vicinity of the methanogens may be higher than the H_2 concentration in equilibrium with the headspace. The best fit between the net carbon isotopic fractionation in methanogenesis ($^{13}\varepsilon_{\mathrm{CO_2\text{-}CH_4}}$) measured in

laboratory co-cultures and predicted in our model is obtained at in-situ H_2 concentrations that are approximately five times higher than the concentration at equilibrium with the headspace.

Energy conservation

Methanogens conserve chemical energy by coupling the exergonic methyl-group transfer by the Mtr-catalyzed reaction to export of Na^+ ions out of the cell:

$$\text{CH}_3\text{-H}_4\text{MPT} + \text{HS-CoM} + x\,\text{Na}^+_{\text{in}} \rightleftarrows \text{CH}_3\text{-SCoM} + \text{H}_4\text{MPT} + x\,\text{Na}^+_{\text{out}}\,, \tag{9}$$

where x is the stoichiometric coefficient for Na^+ translocation per cycle of the reaction. Na^+ translocation generates an electrochemical gradient, which is used to phosphorylate ADP to ATP by a proton- or sodium-driven ATPase (76). Hydrogenotrophic organisms without membrane-associated methanophenazines, such as *M. thermoautotrophicus*, have an ATP yield (Y_{ATP}) of 0.5 mole ATP per mole methane under optimal growth conditions (47). The standard transformed Gibbs free energy of ATP production under physiological conditions ($\Delta G'^{m}_{r,ATP}$) is +43.5 kJ (77), and thus 0.5 moles of ATP require an electrochemical gradient of at least −22 kJ. We assume that the cells use the minimal electrochemical potential possible, so the x in Eq. 9 is equivalent to Y_{ATP}. Based on the observations that the minimal threshold for methanogenic activity is ≈ -10 $\text{kJ}\,\text{mol}^{-1}$(47), we estimate that under non-optimal growth conditions Y_{ATP} is closer to 0.2, and we thus use a default Y_{ATP} value of 0.2. The value of Y_{ATP} affects the reversibility of the Mtr-catalyzed reaction, which is calculated by:

$$1 - \frac{[\text{CH}_3\text{-SCoM}][\text{H}_4\text{MPT}]}{[\text{CH}_3\text{-H}_4\text{MPT}][\text{HS-CoM}]} \times \exp\left(\frac{\Delta G'^{0}_{r,Mtr} + Y_{ATP} \times \Delta G'^{m}_{r,ATP}}{RT}\right)\,. \tag{10}$$

Thus, the choice of Y_{ATP} controls the relative expression of the KFF and EFF of the Mcr-catalyzed reaction, and consequently, the net fractionation of the entire pathway. Importantly, the choice of Y_{ATP} value also sets the smallest ΔG_{net} required for methanogenic activity, which reflects the minimal energetic requirement to produce ATP. For example, with the choice of $Y_{ATP} = 0.2$, there is model methanogenic activity only at $\Delta G_{net} \lessapprox -10\,\text{kJ}\,\text{mol}^{-1}$. This means that ${}^{13}\varepsilon_{CO_2\text{-}CH_4}$, ${}^{2}\varepsilon_{CH_4\text{-}H_2O}$ and clumped isotopologue distributions cannot attain combinations of values typical of isotopic

near-equilibrium (ΔG_{net} between -10 and 0 kJ mol^{-1}). We explore the sensitivity of the model to Y_{ATP} in figs. S13-S15. The effect is most noticeable on $^{13}\varepsilon_{CO_2\text{-}CH_4}$ where a smaller Y_{ATP} value (0.1) induces an earlier departure of the Mtr-catalyzed reaction from equilibrium, which results in a smaller peak in $^{13}\varepsilon_{CO_2\text{-}CH_4}$ values relative to the default Y_{ATP} value of 0.2. A larger Y_{ATP} value (0.3) induces a later departure of the Mtr-catalyzed reaction from equilibrium, which causes a larger peak to larger-than-equilibrium $^{13}\varepsilon_{CO_2\text{-}CH_4}$ values. A best fit between the model and culture experiments is obtained with Y_{ATP} of 0.2.

Enzyme kinetic parameters

The enzyme K_M values of ten metabolites were absent in the literature. Based on the observation that K_M values in various organisms are normally distributed (78), we generated distributions for the missing K_M values. Wherever possible, we determined the mean and standard deviations of these prior distributions based on metabolite-specific K_M values from other enzymes deposited in the BRENDA database (79). We used the model-measurement mismatch to produce posterior distributions for these K_M values, with the following procedure: (*i*) Run the metabolic model 10^4 times, drawing the missing parameters from prior distributions (table S5). (*ii*) Weigh the K_M value drawn from the prior distribution by the model-experimental mismatch of the biomass-specific methanogenesis rate, which were measured for cells grown under optimal conditions in varying H_2 concentrations (36). The weight was defined as the inverse of the squared sum of squared errors ($1/SSE^2$) (fig. S2). (*iii*) Run the metabolic model with the weighted posterior distributions. In the isotopic model, we used the median K_M values from the posterior distributions, which we refer to in the various figures as 'calibrated distributions' (table S5).

The maximal rate capacity V^+ (Eq. 3) is a product of an enzyme's turnover rates (k^+_{cat}) and its concentration ([E]). Enzyme levels are mostly unknown, and to circumvent this we used rate capacities determined *in-vitro* in pure culture crude cell extracts (V^+_{vit}), which provide approximate values of $k^+_{cat} \times$ [E] of all enzymes in the pathway (we explore the sensitivity to these values in figures S13-S15). There were no V^+ values that were completely missing from the literature.

Although this approach avoids the need to prescribe [E] and k^+_{cat} values, V^+_{vit} does not necessarily reflect *in-vivo* rate capacities (V^+_{viv}). To account for the difference between *in-vitro* and *in-vivo* conditions we used a scaling factor:

$$U_{viv/vit} = \frac{[\mathrm{E}]_{viv} \times k^+_{cat,viv}}{[\mathrm{E}]_{vit} \times k^+_{cat,vit}}. \tag{11}$$

Assuming that $k^+_{cat,vit} \approx k^+_{cat,viv}$, this term reduces to $U_{viv/vit} = [\mathrm{E}]_{viv}/[\mathrm{E}]_{vit}$, which implies that this scaling factor is essentially a ratio of the active enzyme concentrations of *in-vitro* and *in-vivo* conditions. We also assumed that this ratio is uniform across all enzymes. To determine $U_{viv/vit}$ we used the model-experiment mismatch, as was described for the K_M values (fig. S2). We found that using a $U_{viv/vit}$ value of $\approx$11 yields the best match between the model and experimental results of biomass-specific methanogenesis rates.

Temperature effects on methanogenesis rates

The V^+ values in the model were obtained from crude cell extracts that were mostly cultured at 60°C, and we have only limited information to determine the dependence of V^+ values on temperature. Generally, temperature is expected to affect the activity of individual enzymes, the thermodynamics of the individual reactions, and likely other whole-organism properties. The activity of single enzymes has well-described temperature dependences, with a typical peak due to changes in the heat capacity of the enzyme (80, 81). The effect of temperature on the net rate of individual reactions in the pathway is built into our metabolic model through the thermodynamic term in Eq. 3 ($1 - e^{\Delta \mathrm{G}_i/\mathrm{RT}}$). Uncertainty in the temperature dependence of $\Delta \mathrm{G}'^0_\mathrm{r}$ values that have not been determined experimentally currently precludes incorporation of this temperature dependence of net rates in the model.

The effect of temperature on whole-organism activity is more difficult to evaluate, as organisms adapt to maximize activity at different temperatures by a suite of physiological changes, for example, by controlling enzyme expression rates, the spatial density of membrane transporters and the composition of membranes, with effects on membrane permeability. We account for the coupled dependence of enzyme activity and whole-organism adaptations by assigning an Arrhenius type

temperature dependence term ($Q_{10}^{V^+}$) that determines the V^+ for a given temperature:

$$V_2^+ = V_1^+ \times \left(Q_{10}^{V^+}\right)^{\Delta T/10°C}, \tag{12}$$

where ΔT is the temperature difference. We reemphasize that currently there are no estimates of the actual magnitude of $Q_{10}^{V^+}$. We found that when $Q_{10}^{V^+}$ is assigned a value of unity (i.e., csMR increases with temperature only due to temperature effects on the thermodynamic drive), csMR increases by up to three orders of magnitude between 0°C and 60°C when ΔG_{net} is a small negative number (≈ -15 kJ mol^{-1}). This is equivalent to an increase in csMR by a factor of $\approx$3.2 per 10°C warming. At large negative ΔG_{net}, csMR is almost independent of temperature, as the thermodynamic drive is close to unity irrespective of temperature (fig. S10, solid lines). A $Q_{10}^{V^+}$ value greater than unity results in a higher temperature sensitivity of csMR. For example, assigning a $Q_{10}^{V^+}$ value of 1.5 generates csMR that is $\sim$4 orders of magnitude lower at 0°C than at 60°C when ΔG_{net} is a small negative value (equivalent to a factor of $\approx$4.6 increase per 10°C warming), and approximately tenfold lower when ΔG_{net} has a large negative value (fig. S10, dotted lines). In the model we used a default value for $Q_{10}^{V^+}$ of 1, resulting in a "whole-organism" increase in csMR by a factor of $\approx$3.2 for every 10°C warming. We note that choosing a $Q_{10}^{V^+}$ of 1 does not imply that the activity of single enzymes is independent of temperature, but rather that the maximal rate capacity of enzymatically catalyzed reactions may be approximately invariant across temperatures in organisms that are adapted to those temperatures.

Isotopic model parameters

The temperature-dependent isotope EFFs that are associated with each of the steps in the hydrogenotrophic methanogenesis pathway were calculated using density functional theory (DFT) at the M06-L/def2-TZVP level of theory with the SMD implicit solvation model (44, 82). The KFFs were determined experimentally only for Mcr (43). To account for missing KFFs we randomly sampled their values from prior uniform distributions 10^6 times. We included both primary and secondary isotopic effects (α_p^+ and α_s^+, respectively). Primary isotopic effects are due to the breaking or formation of a bond directly with the atom of interest, and secondary isotopic effects

are due to breaking or formation of an adjacent bond. Secondary KFFs are usually smaller than primary KFFs. We weighted the combinations of KFFs drawn from the prior distributions by the model-experimental mismatch, expressed as the inverse of the squared sum of squared errors ($1/\mathrm{SSE}^2$), to generate posterior distributions of the KFFs, which were then used in the model, in a procedure similar to that used to determine the missing K_M and $U_{viv/vit}$ values. We assumed that KFFs are similar between the different temperatures as we found that separately calibrating the model at each temperature yielded very similar posterior distributions. The reverse KFF for each simulation is calculated from the forward KFF and the temperature-dependent EFF, as required by relation $\alpha^{\mathrm{eq}} = \alpha^{-}/\alpha^{+}$. This yields slightly different posterior distributions of the reverse KFFs between the two temperatures (fig. S16). We assumed normal KFFs (i.e., the light isotopologues react faster than the heavy isotopologues, $\alpha < 1$) for both carbon and hydrogen isotopes, and assigned $\alpha_p^{+} \in (0.4, 1)$ ($\alpha_p^{+} \in (0.2, 1)$ for the Mvh/Hdr-catalyzed reaction) and $\alpha_s^{+} \in (0.6, 1)$ for hydrogen isotopes, and $\alpha^{+} \in (0.935, 1)$ for carbon isotopes. Notably, optimal model-measurement fits were obtained with an inverse KFF (i.e., $\alpha^{+} > 1$) for the Mvh/Hdr-catalyzed back reaction. While normal KFFs are more common, in some cases inverse KFFs emerge, often in a multistep enzymatic reaction that is treated as one composite reaction. In such reactions, chemical and isotopic equilibrium between reaction intermediates before the rate determining steps may lead to an overall (apparent) inverse KFF, even if the rate determining step itself has a normal KFF (83, 84). The KFFs of Mcr were assigned distributions based on the experimental measurements (43). The carbon KFF was drawn from a normal distribution with a mean of 0.9615 and a standard deviation of 0.01, and the hydrogen KFFs were drawn from normal distributions (for α_p^{+} with a mean of 0.41 and a standard deviation of 0.04, and for α_s^{+} with a mean of 0.85 and a standard deviation of 0.035).

The posterior distributions of the KFFs (fig. S3) serve as a sensitivity analysis of the model. Posterior distributions that are similar to the prior distributions indicate insensitivity to the model parameter, in this case, the KFF value. For carbon isotopes, the model shows sensitivity to the KFFs of Fmd, Ftr and Mtr with smallest-mismatch values of $-27‰$, $-32‰$, and $-28‰$ at mesophilic

conditions, respectively. This sensitivity is in line with our observations of the reactions that determine the trajectory of ${}^{13}\varepsilon_{CO_2\text{-}CH_4}$ departure from equilibrium. For hydrogen isotopes, the model shows sensitivity to most of the primary KFFs, and to the secondary KFFs of Fmd and Mtr. Notably, the primary KFFs of Mtd and Frh tend to be small (i.e., closer to unity), with median values between $\approx -300‰$ and $\approx -260‰$.

The KFFs of the clumped isotopologues are expressed as deviations from the product of the KFFs of the singly-substituted isotopologues, and are denoted by ${}^{x,y}\gamma$ where x and y are the rare isotopes and ${}^{x,y}\gamma = {}^{x,y}\alpha^{+} / ({}^{x}\alpha^{+} \times {}^{y}\alpha^{+})$. The γ values are typically small and close to unity (23). We drew primary and secondary γ values (γ_p and γ_s, respectively) from uniform distributions: ${}^{13,2}\gamma_p \in (0.997, 1)$ and ${}^{13,2}\gamma_s \in (1, 1)$ for ^{13}C-D clumping, and ${}^{2,2}\gamma_p \in (0.994, 1)$ and ${}^{2,2}\gamma_s \in (1, 1)$ for double D clumping, which are similar to ranges that were explored in previous works (24).

Simulating methanogenesis in energy-limited conditions

The metabolic parameters that we used to explore isotopic fractionation in methanogenesis were curated from cell cultures grown under optimal conditions. However, methanogens tightly regulate gene expression under energy-limiting conditions, resulting in shifts in enzyme specific activities (e.g., 35, 36, 54, 85, 86). Specifically, prolonged H_2 limitation promotes higher activities of Frh, Mvh/Hdr and the Mcr I isoenzyme, in parallel to a decrease in the activity of Mcr II (35, 36). Mcr I has a higher affinity to the substrates CH_3-SCoM and HS-CoB relative to Mcr II, allowing the cells to increase the cell-specific respiration rate when H_2 becomes limiting (35, 87, 88). Therefore, in the simulations of methanogenesis in natural, energy-limited environments we used enzyme activities measured in crude extracts from cells that were grown under conditions favoring Mcr I activity (36) with K_M values of Mcr I (table S2). In laboratory cultures, cells under energy limitation decrease their volume in a matter of days or weeks, and a similar phenomenon was observed when comparing cell communities in energy-replete *vs.* energy-deprived environmental settings (89). Thus, we use a cellular volume smaller by a factor of two from the default value (2 fL cell^{-1} *vs.* 1 fL cell^{-1}).

Acknowledgments

J.G. acknowledges support from the Sustainability and Energy Research Initiative (SAERI) of the Weizmann Institute of Science. Q.J. is supported by NSF award EAR-1636815.

Author contributions

J.G. and I.H. conceived the study, developed and analyzed the metabolic-isotopic model, and wrote the initial draft. Q.J. developed the metabolic model. All authors contributed to the writing.

Competing Interests

The authors declare that they have no competing interests.

Data Availability

All data needed to evaluate the conclusions in the paper are present in the paper and/or the Supplementary Materials.

References

[1] M. Saunois, *et al.*, The global methane budget 2000–2012. *Earth Syst. Sci. Data* **8**, 697–751 (2016).

[2] S. Schwietzke, O. A. Sherwood, L. M. P. Bruhwiler, J. B. Miller, G. Etiope, E. J. Dlugokencky, S. E. Michel, V. A. Arling, B. H. Vaughn, J. W. C. White, P. P. Tans, Upward revision of global fossil fuel methane emissions based on isotope database. *Nature* **538**, 88–91 (2016).

[3] Z. Lyu, N. Shao, T. Akinyemi, W. B. Whitman, Methanogenesis. *Current Biology* **28**, R727-R732 (2018).

[4] M. J. Whiticar, Carbon and hydrogen isotope systematics of bacterial formation and oxidation of methane. *Chem. Geol.* **161**, 291–314 (1999).

[5] E. G. Nisbet, E. J. Dlugokencky, M. R. Manning, D. Lowry, R. E. Fisher, J. L. France, S. E. Michel, J. B. Miller, J. W. C. White, B. Vaughn, P. Bousquet, J. A. Pyle, N. J. Warwick, M. Cain, R. Brownlow, G. Zazzeri, M. Lanoisellé, A. C. Manning, E. Gloor, D. E. J. Worthy, E.-G. Brunke, C. Labuschagne, E. W. Wolff, A. L. Ganesan, Rising atmospheric methane: 2007-2014 growth and isotopic shift. *Glob. Biogeochem. Cycles* **30**, 1356–1370 (2016).

[6] K. J. Murata, I. Friedman, M. Cremer, Geochemistry of diagenetic dolomites in Miocene marine formations of California and Oregon, *Professional Paper 724-C*, United States Geological Survey (1972).

[7] Y. Bottinga, Calculated fractionation factors for carbon and hydrogen isotope exchange in the system calcite-carbon dioxide-graphite-methane-hydrogen-water vapor. *Geochim. Cosmochim. Acta* **33**, 49–64 (1969).

[8] L. M. Games, J. M. Hayes, *Proceedings of the 2nd International Symposium on Environ-*

mental Biogeochemistry, J. O. Nriagu, ed. (Science Publishers, Ann Arbor Mi, 1976), vol. 1, pp. 51–73.

[9] J. W. Smith, K. W. Gould, D. Rigby, The stable isotope geochemistry of Australian coals. *Organic Geochemistry* **3**, 111–131 (1981).

[10] L. M. Games, J. Hayes, R. P. Gunsalus, Methane-producing bacteria: Natural fractionations of the stable carbon isotopes. *Geochim. Cosmochim. Acta* **42**, 1295–1297 (1978).

[11] G. Fuchs, R. Thauer, H. Ziegler, W. Stichler, Carbon isotope fractionation by Methanobacterium thermoautotrophicum. *Arch. Microbiol.* **120**, 135–139 (1979).

[12] S. S. Belyaev, R. Wolkin, W. R. Kenealy, M. J. Deniro, S. Epstein, J. G. Zeikus, Methanogenic bacteria from the bondyuzhskoe oil field: General characterization and analysis of stable-carbon isotopic fractionation. *Appl. Environ. Microbiol.* **45**, 691–7 (1983).

[13] M. Balabane, E. Galimov, M. Hermann, R. Létolle, Hydrogen and carbon isotope fractionation during experimental production of bacterial methane. *Org. Geochem.* **11**, 115–119 (1987).

[14] R. Botz, H. D. Pokojski, M. Schmitt, M. Thomm, Carbon isotope fractionation during bacterial methanogenesis by CO2 reduction. *Org. Geochem.* **25**, 255–262 (1996).

[15] A. M. Zyakun, V. A. Bondar, K. S. Laurinavichus, O. V. Shipin, S. S. Belyaev, M. V. Ivanov, Fractionation of carbon isotopes under the growth of methane-producing bacteria on various substrates. *Mikrobiol. Zhurnal* **50**, 16–22 (1988).

[16] D. L. Valentine, A. Chidthaisong, A. Rice, W. S. Reeburgh, S. C. Tyler, Carbon and hydrogen isotope fractionation by moderately thermophilic methanogens. *Geochim. Cosmochim. Acta* **68**, 1571–1590 (2004).

[17] H. Penning, C. M. Plugge, P. E. Galand, R. Conrad, Variation of carbon isotope fractionation in hydrogenotrophic methanogenic microbial cultures and environmental samples at different energy status. *Glob. Change Biol.* **11**, 2103–2113 (2005).

[18] K. Takai, K. Nakamura, T. Toki, U. Tsunogai, M. Miyazaki, J. Miyazaki, H. Hirayama, S. Nakagawa, T. Nunoura, K. Horikoshi, Cell proliferation at 122 degrees C and isotopically heavy CH4 production by a hyperthermophilic methanogen under high-pressure cultivation. *Proc. Natl. Acad. Sci. U. S. A.* **105**, 10949–54 (2008).

[19] S. Hattori, H. Nashimoto, H. Kimura, K. Koba, K. Yamada, M. Shimizu, H. Watanabe, M. Yoh, N. Yoshida, Hydrogen and carbon isotope fractionation by thermophilic hydrogenotrophic methanogens from a deep aquifer under coculture with fermenters. *Geochem. J.* **46**, 193–200 (2012).

[20] T. Okumura, S. Kawagucci, Y. Saito, Y. Matsui, K. Takai, H. Imachi, Hydrogen and carbon isotope systematics in hydrogenotrophic methanogenesis under H2-limited and H2-enriched conditions: Implications for the origin of methane and its isotopic diagnosis. *Prog. Earth Planet. Sci.* **3**, 14 (2016).

[21] B. D. Topçuoğlu, C. Meydan, T. B. Nguyen, S. Q. Lang, J. F. Holden, Growth Kinetics, Carbon Isotope Fractionation, and Gene Expression in the Hyperthermophile Methanocaldococcus jannaschii during Hydrogen-Limited Growth and Interspecies Hydrogen Transfer. *Appl. Environ. Microbiol.* **85**, 1–14 (2019).

[22] D. A. Stolper, A. Martini, M. Clog, P. Douglas, S. Shusta, D. Valentine, A. Sessions, J. Eiler, Distinguishing and understanding thermogenic and biogenic sources of methane using multiply substituted isotopologues. *Geochim. Cosmochim. Acta* **161**, 219–247 (2015).

[23] D. T. Wang, D. S. Gruen, B. S. Lollar, K.-U. Hinrichs, L. C. Stewart, J. F. Holden, A. N. Hristov, J. W. Pohlman, P. L. Morrill, M. Könneke, K. B. Delwiche, E. P. Reeves, C. N.

Sutcliffe, D. J. Ritter, J. S. Seewald, J. C. McIntosh, H. F. Hemond, M. D. Kubo, D. Cardace, T. M. Hoehler, S. Ono, Nonequilibrium clumped isotope signals in microbial methane. *Science* **348**, 428–431 (2015).

[24] X. Cao, H. Bao, Y. Peng, A kinetic model for isotopologue signatures of methane generated by biotic and abiotic CO2 methanation. *Geochim. Cosmochim. Acta* **249**, 59–75 (2019).

[25] B. A. Wing, I. Halevy, Intracellular metabolite levels shape sulfur isotope fractionation during microbial sulfate respiration. *Proc. Natl. Acad. Sci. U. S. A.* **111**, 18116–25 (2014).

[26] E. Noor, A. Flamholz, W. Liebermeister, A. Bar-Even, R. Milo, A note on the kinetics of enzyme action: A decomposition that highlights thermodynamic effects. *FEBS Lett.* **587**, 2772–7 (2013).

[27] R. A. Alberty, *Thermodynamics of Biochemical Reactions* (John Wiley & Sons, Inc., Hoboken, NJ, USA, 2003).

[28] A.-K. Kaster, J. Moll, K. Parey, R. K. Thauer, Coupling of ferredoxin and heterodisulfide reduction via electron bifurcation in hydrogenotrophic methanogenic archaea. *PNAS* **108**, 2981–6 (2011).

[29] T. Watanabe, O. Pfeil-Gardiner, J. Kahnt, J. Koch, S. Shima, B. J. Murphy, Three-megadalton complex of methanogenic electron-bifurcating and CO2-fixing enzymes. *Science* (2021).

[30] L. M. I. de Poorter, W. J. Geerts, J. T. Keltjens, Hydrogen concentrations in methane-forming cells probed by the ratios of reduced and oxidized coenzyme F420. *Microbiology* **151**, 1697–1705 (2005).

[31] C. Walsh, Naturally occurring 5-deazaflavin coenzymes: Biological redox roles. *Acc. Chem. Res.* **19**, 216–221 (1986).

[32] F. Jacobson, C. Walsh, Properties of 7,8-Didemethyl-8-hydroxy-5-deazaflavins Relevant to Redox Coenzyme Function in Methanogen Metabolism. *Biochemistry* **23**, 979–988 (1984).

[33] L. D. Eirich, G. D. Vogels, R. S. Wolfe, Distribution of coenzyme F420 and properties of its hydrolytic fragments. *J. Bacteriol.* **140**, 20–7 (1979).

[34] L. M. I. de Poorter, W. G. Geerts, A. P. R. Theuvenet, J. T. Keltjens, Bioenergetics of the formyl-methanofuran dehydrogenase and heterodisulfide reductase reactions in Methanothermobacter thermautotrophicus. *Eur. J. Biochem.* **270**, 66–75 (2002).

[35] P. Vermeij, J. L. Pennings, S. M. Maassen, J. T. Keltjens, G. D. Vogels, Cellular levels of factor 390 and methanogenic enzymes during growth of Methanobacterium thermoautotrophicum deltaH. *J. Bacteriol.* **179**, 6640–8 (1997).

[36] J. L. Pennings, P. Vermeij, L. M. de Poorter, J. T. Keltjens, G. D. Vogels, Adaptation of methane formation and enzyme contents during growth of Methanobacterium thermoautotrophicum (strain ΔH) in a fed-batch fermentor. *Antonie van Leeuwenhoek* **77**, 281–291 (2000).

[37] J. Bassham, G. Krause, Free energy changes and metabolic regulation in steady-state photosynthetic carbon reduction. *Biochim. Biophys. Acta BBA - Bioenerg.* **189**, 207–221 (1969).

[38] D. A. Beard, H. Qian, Relationship between thermodynamic driving force and one-way fluxes in reversible processes. *PloS one* **2**, e144 (2007).

[39] C. Rees, A steady-state model for sulphur isotope fractionation in bacterial reduction processes. *Geochim. Cosmochim. Acta* **37**, 1141–1162 (1973).

[40] M. A. Iron, J. Gropp, Cost-Effective Density Functional Theory (DFT) Calculations of Equilibrium Isotopic Fractionation in Large Organic Molecules. *Phys. Chem. Chem. Phys.* pp. 17555–17570 (2019).

[41] H. Yoshioka, S. Sakata, Y. Kamagata, Hydrogen isotope fractionation by Methanothermobacter thermoautotrophicus in coculture and pure culture conditions. *Geochim. Cosmochim. Acta* **72**, 2687–2694 (2008).

[42] A. C. Turner, R. Korol, D. L. Eldridge, M. Bill, M. E. Conrad, T. F. Miller, D. A. Stolper, Experimental and theoretical determinations of hydrogen isotopic equilibrium in the system CH4-H2-H2O from 3 to 200°C. *Geochimica et Cosmochimica Acta* **1**, 1 (2021).

[43] S. Scheller, M. Goenrich, R. K. Thauer, B. Jaun, Methyl-coenzyme M reductase from methanogenic archaea: Isotope effects on the formation and anaerobic oxidation of methane. *J. Am. Chem. Soc.* **135**, 14975–84 (2013).

[44] J. Gropp, M. A. Iron, I. Halevy, Theoretical estimates of equilibrium carbon and hydrogen isotope effects in microbial methane production and anaerobic oxidation of methane. *Geochimica et Cosmochimica Acta* **295**, 237–264 (2021).

[45] H. M. Miller, N. Chaudhry, M. E. Conrad, M. Bill, S. H. Kopf, A. S. Templeton, Large carbon isotope variability during methanogenesis under alkaline conditions. *Geochim. Cosmochim. Acta* **237**, 18–31 (2018).

[46] D. B. Nothaft, A. S. Templeton, J. H. Rhim, D. T. Wang, J. Labidi, H. M. Miller, E. S. Boyd, J. M. Matter, S. Ono, E. D. Young, S. H. Kopf, P. B. Kelemen, M. E. Conrad, Geochemical, biological and clumped isotopologue evidence for substantial microbial methane production under carbon limitation in serpentinites of the Samail Ophiolite, Oman. *J. Geophys. Res. Biogeosciences* **NA**, e2020JG006025 (2021).

[47] R. K. Thauer, A.-K. Kaster, H. Seedorf, W. Buckel, R. Hedderich, Methanogenic archaea: Ecologically relevant differences in energy conservation. *Nat. Rev. Microbiol.* **6**, 579–591 (2008).

[48] S. W. Ragsdale, M. Kumar, Nickel-Containing Carbon Monoxide Dehydrogenase/Acetyl-CoA Synthase,. *Chem. Rev.* **96**, 2515–2540 (1996).

[49] P. G. Simpson, W. B. Whitman, Anabolic pathways in methanogens. *Methanogenesis* (Springer, 1993), pp. 445–472.

[50] M. J. Alperin, T. M. Hoehler, Anaerobic methane oxidation by archaea/sulfate-reducing bacteria aggregates: 2. Isotopic constraints. *Am J Sci* **309**, 958–984 (2009).

[51] K. L. Londry, K. G. Dawson, H. D. Grover, R. E. Summons, A. S. Bradley, Stable carbon isotope fractionation between substrates and products of Methanosarcina barkeri. *Org. Geochem.* **39**, 608–621 (2008).

[52] T. B. Nguyen, B. D. Topçuoğlu, J. F. Holden, D. E. LaRowe, S. Q. Lang, Lower hydrogen flux leads to larger carbon isotopic fractionation of methane and biomarkers during hydrogenotrophic methanogenesis. *Geochimica et Cosmochimica Acta* **271**, 212–226 (2020).

[53] S. Kawagucci, M. Kobayashi, S. Hattori, K. Yamada, Y. Ueno, K. Takai, N. Yoshida, Hydrogen isotope systematics among H2–H2O–CH4 during the growth of the hydrogenotrophic methanogen Methanothermobacter thermautotrophicus strain ΔH. *Geochim. Cosmochim. Acta* **142**, 601–614 (2014).

[54] C. Afting, E. Kremmer, C. Brucker, A. Hochheimer, R. K. Thauer, Regulation of the synthesis of H2-forming methylenetetrahydromethanopterin dehydrogenase (Hmd) and of HmdII and HmdIII in Methanothermobacter marburgensis. *Arch. Microbiol.* **174**, 225–232 (2000).

[55] P. M. Vignais, H/D exchange reactions and mechanistic aspects of the hydrogenases. *Coordination Chemistry Reviews* **249**, 1677–1690 (2005).

[56] S. Walter, S. Laukenmann, A. J. M. Stams, M. K. Vollmer, G. Gleixner, T. Röckmann, The stable isotopic signature of biologically produced molecular hydrogen (H_2). *Biogeosciences* **9**, 4115–4123 (2012).

[57] J. H. Rolston, J. Den Hartog, J. P. Butler, The deuterium isotope separation factor between hydrogen and liquid water. *J. Phys. Chem.* **80**, 1064–1067 (1976).

[58] D. A. Stolper, M. Lawson, C. L. Davis, A. A. Ferreira, E. V. Santos Neto, G. S. Ellis, M. D. Lewan, A. M. Martini, Y. Tang, M. Schoell, A. L. Sessions, J. M. Eiler, Formation temperatures of thermogenic and biogenic methane. *Science* **344**, 1500–1503 (2014).

[59] P. M. Douglas, D. A. Stolper, J. M. Eiler, A. L. Sessions, M. Lawson, Y. Shuai, A. Bishop, O. G. Podlaha, A. A. Ferreira, E. V. Santos Neto, M. Niemann, A. S. Steen, L. Huang, L. Chimiak, D. L. Valentine, J. Fiebig, A. J. Luhmann, W. E. Seyfried, G. Etiope, M. Schoell, W. P. Inskeep, J. J. Moran, N. Kitchen, Methane clumped isotopes: Progress and potential for a new isotopic tracer. *Org. Geochem.* **113**, 262–282 (2017).

[60] L. Y. Yeung, Combinatorial effects on clumped isotopes and their significance in biogeochemistry. *Geochim. Cosmochim. Acta* **172**, 22–38 (2016).

[61] T. Röckmann, M. E. Popa, M. C. Krol, M. E. G. Hofmann, Statistical clumped isotope signatures. *Sci. Rep.* **6**, 31947 (2016).

[62] L. Taenzer, J. Labidi, A. L. Masterson, X. Feng, D. Rumble, E. D. Young, W. D. Leavitt, Low Δ12CH2D2 values in microbialgenic methane result from combinatorial isotope effects. *Geochimica et Cosmochimica Acta* **285**, 225–236 (2020).

[63] J. H. Rhim, Experimental investigations of isotopologue fractionation during microbial methanogenesis, Ph.D. thesis, Massachusetts Institute of Technology (2020).

[64] D. S. Vinson, N. E. Blair, A. M. Martini, S. Larter, W. H. Orem, J. C. McIntosh, Microbial methane from in situ biodegradation of coal and shale: A review and reevaluation of hydrogen and carbon isotope signatures. *Chem. Geol.* **453**, 128–145 (2017).

[65] J. J. Jautzy, P. M. J. Douglas, H. Xie, J. M. Eiler, I. D. Clark, CH4 isotopic ordering records ultra-slow hydrocarbon biodegradation in the deep subsurface. *Earth and Planetary Science Letters* **562**, 116841 (2021).

[66] N. Zhang, G. T. Snyder, M. Lin, M. Nakagawa, A. Gilbert, N. Yoshida, R. Matsumoto, Y. Sekine, Doubly substituted isotopologues of methane hydrate (13CH3D and 12CH2D2):

Implications for methane clumped isotope effects, source apportionments and global hydrate reservoirs. *Geochimica et Cosmochimica Acta* **315**, 127–151 (2021).

[67] R. Conrad, T. J. Phelps, J. G. Zeikus, Gas metabolism evidence in support of the juxtaposition of hydrogen-producing and methanogenic bacteria in sewage sludge and lake sediments. *Appl. Environ. Microbiol.* **50**, 595–601 (1985).

[68] E. Giraldo-Gomez, S. Goodwin, M. S. Switzenbaum, Influence of mass transfer limitations on determination of the half saturation constant for hydrogen uptake in a mixed-culture CH4-producing enrichment. *Biotechnol. Bioeng.* **40**, 768–76 (1992).

[69] Y.-S. Lin, V. B. Heuer, T. Goldhammer, M. Y. Kellermann, M. Zabel, K.-U. Hinrichs, Towards constraining H2 concentration in subseafloor sediment: A proposal for combined analysis by two distinct approaches. *Geochimica et Cosmochimica Acta* **77**, 186–201 (2012).

[70] J. A. Bradley, S. Arndt, J. P. Amend, E. Burwicz, A. W. Dale, M. Egger, D. E. LaRowe, Widespread energy limitation to life in global subseafloor sediments. *Sci. Adv.* **6**, eaba0697 (2020).

[71] C. K. Paull, T. D. Lorenson, W. S. Borowski, W. Ussler III, K. Olsen, N. M. Rodriguez, Isotopic Composition of CH4, CO2 Species, and Sedimentary Organic Matter Within Samples From the Blake Ridge: Gas Source Implications. *Proc. Ocean Drill. Program Sci. Results* **164**, 67–78 (2000).

[72] J. W. Pohlman, M. Kaneko, V. B. Heuer, R. B. Coffin, M. Whiticar, Methane sources and production in the northern Cascadia margin gas hydrate system. *Earth and Planetary Science Letters* **287**, 504–512 (2009).

[73] G. Wegener, J. Gropp, H. Taubner, I. Halevy, M. Elvert, Sulfate-dependent reversibility of intracellular reactions explains the opposing isotope effects in the anaerobic oxidation of methane. *Sci. Adv.* **7**, eabe4939 (2021).

[74] M. K. Lloyd, E. Trembath-Reichert, K. S. Dawson, S. J. Feakins, M. Mastalerz, V. J. Orphan, A. L. Sessions, J. M. Eiler, Methoxyl stable isotopic constraints on the origins and limits of coal-bed methane. *Science* **374**, 894–897 (2021).

[75] A. Missner, P. Kügler, S. M. Saparov, K. Sommer, J. C. Mathai, M. L. Zeidel, P. Pohl, Carbon dioxide transport through membranes. *J. Biol. Chem.* **283**, 25340–7 (2008).

[76] U. Deppenmeier, V. Müller, Life close to the thermodynamic limit: How methanogenic archaea conserve energy. *Results Probl. Cell Differ.* **45**, 123–52 (2008).

[77] A. Flamholz, E. Noor, A. Bar-Even, R. Milo, eQuilibrator–the biochemical thermodynamics calculator. *Nucleic Acids Res.* **40**, D770-5 (2012).

[78] A. Bar-Even, E. Noor, Y. Savir, W. Liebermeister, D. Davidi, D. S. Tawfik, R. Milo, The Moderately Efficient Enzyme: Evolutionary and Physicochemical Trends Shaping Enzyme Parameters. *Biochemistry* **50**, 4402–4410 (2011).

[79] A. Chang, L. Jeske, S. Ulbrich, J. Hofmann, J. Koblitz, I. Schomburg, M. Neumann-Schaal, D. Jahn, D. Schomburg, BRENDA, the ELIXIR core data resource in 2021: New developments and updates. *Nucleic Acids Research* **49**, D498-D508 (2021).

[80] J. K. Hobbs, W. Jiao, A. D. Easter, E. J. Parker, L. A. Schipper, V. L. Arcus, Change in Heat Capacity for Enzyme Catalysis Determines Temperature Dependence of Enzyme Catalyzed Rates. *ACS Chem. Biol.* **8**, 2388–2393 (2013).

[81] L. A. Schipper, J. K. Hobbs, S. Rutledge, V. L. Arcus, Thermodynamic theory explains the temperature optima of soil microbial processes and high Q10 values at low temperatures. *Glob. Change Biol.* **20**, 3578–3586 (2014).

[82] J. Gropp, M. A. Iron, I. Halevy, Corrigendum to "Theoretical estimates of equilibrium carbon and hydrogen isotope effects in microbial methane production and anaerobic oxidation of methane" [Geochim. Cosmochim. Acta 295 (2021) 237–264]. *Geochimica et Cosmochimica Acta* **306**, 386–389 (2021).

[83] A. Sattler, Hydrogen/Deuterium (H/D) Exchange Catalysis in Alkanes. *ACS Catal.* **8**, 2296–2312 (2018).

[84] M. Gómez-Gallego, M. A. Sierra, Kinetic isotope effects in the study of organometallic reaction mechanisms. *Chem. Rev.* **111**, 4857–963 (2011).

[85] E. L. Hendrickson, A. K. Haydock, B. C. Moore, W. B. Whitman, J. A. Leigh, Functionally distinct genes regulated by hydrogen limitation and growth rate in methanogenic Archaea. *Proc. Natl. Acad. Sci. U. S. A.* **104**, 8930–4 (2007).

[86] S. Kato, T. Kosaka, K. Watanabe, Comparative transcriptome analysis of responses of Methanothermobacter thermautotrophicus to different environmental stimuli. *Environ. Microbiol.* **10**, 893–905 (2008).

[87] L. G. Bonacker, S. Baudner, R. K. Thauer, Differential expression of the two methyl-coenzyme M reductases in Methanobacterium thermoautotrophicum as determined immunochemically via isoenzyme-specific antisera. *Eur. J. Biochem.* **206**, 87–92 (1992).

[88] L. G. Bonacker, S. Baudner, E. Mörschel, R. Böcher, R. K. Thauer, Properties of the two isoenzymes of methyl-coenzyme M reductase in Methanobacterium thermoautotrophicum. *Eur. J. Biochem.* **217**, 587–95 (1993).

[89] M. A. Lever, K. L. Rogers, K. G. Lloyd, J. Overmann, B. Schink, R. K. Thauer, T. M. Hoehler, B. B. Jørgensen, Life under extreme energy limitation: A synthesis of laboratory- and field-based investigations. *FEMS Microbiol Rev* **39**, 688–728 (2015).

[90] J. Kallmeyer, R. Pockalny, R. R. Adhikari, D. C. Smith, S. D'Hondt, Global distribution of microbial abundance and biomass in subseafloor sediment. *Proc. Natl. Acad. Sci.* **109**, 16213–16216 (2012).

[91] C. Petro, P. Starnawski, A. Schramm, K. U. Kjeldsen, Microbial community assembly in marine sediments. *Aquat. Microb. Ecol.* **79**, 177–195 (2017).

[92] T. Hoshino, F. Inagaki, Abundance and distribution of Archaea in the subseafloor sedimentary biosphere. *ISME J.* **13**, 227–231 (2019).

[93] P. A. Bertram, R. K. Thauer, Thermodynamics of the Formylmethanofuran Dehydrogenase Reaction in Methanobacterium Thermoautotrophicum. *Eur. J. Biochem.* **226**, 811–818 (1994).

[94] W. Buckel, R. K. Thauer, Energy conservation via electron bifurcating ferredoxin reduction and proton/Na(+) translocating ferredoxin oxidation. *Biochim. Biophys. Acta* **1827**, 94–113 (2013).

[95] B. E. Maden, Tetrahydrofolate and tetrahydromethanopterin compared: Functionally distinct carriers in C1 metabolism. *Biochem. J.* **350 Pt 3**, 609–29 (2000).

[96] M. Tietze, A. Beuchle, I. Lamla, N. Orth, M. Dehler, G. Greiner, U. Beifuss, Redox Potentials of Methanophenazine and CoB-S-S-CoM, Factors Involved in Electron Transport in Methanogenic Archaea. *ChemBioChem* **4**, 333–335 (2003).

[97] G. Börner, M. Karrasch, R. K. Thauer, Molybdopterin adenine dinucleotide and molybdopterin hypoxanthine dinucleotide in formylmethanofuran dehydrogenase from Methanobacterium thermoautotrophicum (Marburg). *FEBS Lett.* **290**, 31–4 (1991).

[98] P. A. Bertram, M. Karrasch, R. A. Schmitz, R. Bocher, S. P. J. Albracht, R. K. Thauer, Formylmethanofuran dehydrogenases from methanogenic Archaea Substrate specificity, EPR properties and reversible inactivation by cyanide of the molybdenum or tungsten iron-sulfur proteins. *Eur. J. Biochem.* **220**, 477–484 (1994).

[99] M. I. Donnelly, R. S. Wolfe, The role of formylmethanofuran: Tetrahydromethanopterin formyltransferase in methanogenesis from carbon dioxide. *J. Biol. Chem.* **261**, 16653–9 (1986).

[100] J. Breitung, R. K. Thauer, Formylmethanofuran: Tetrahydromethanopterin formyltransferase from Methanosarcina barkeri. Identification of N5-formyltetrahydromethanopterin as the product. *FEBS Lett.* **275**, 226–30 (1990).

[101] A. A. DiMarco, M. I. Donnelly, R. S. Wolfe, Purification and properties of the 5,10-methenyltetrahydromethanopterin cyclohydrolase from Methanobacterium thermoautotrophicum. *J. Bacteriol.* **168**, 1372–7 (1986).

[102] J. Breitung, R. A. Schmitz, K. O. Stetter, R. K. Thauer, N5,N10-Methenyltetrahydromethanopterin cyclohydrolase from the extreme thermophile Methanopyrus kandleri: Increase of catalytic efficiency (kcat/KM) and thermostability in the presence of salts. *Arch. Microbiol.* **156**, 517–524 (1991).

[103] B. W. te Brömmelstroet, C. M. Hensgens, W. J. Geerts, J. T. Keltjens, C. van der Drift, G. D. Vogels, Purification and properties of 5,10-methenyltetrahydromethanopterin cyclohydrolase from Methanosarcina barkeri. *J. Bacteriol.* **172**, 564–71 (1990).

[104] B. Mukhopadhyay, L. Daniels, Aerobic purification of N5,N10-methylenetetrahydromethanopterin dehydrogenase, separated from N5,N10-methenyltetrahydromethanopterin cyclohydrolase, from Methanobacterium thermoautotrophicum strain Marburg. *Can. J. Microbiol.* **35**, 499–507 (1989).

[105] B. te Brömmelstroet, C. M. Hensgens, J. T. Keltjens, C. van der Drift, G. D. Vogels, Purification and characterization of coenzyme F420-dependent 5,10-methylenetetrahydromethanopterin dehydrogenase from Methanobacterium thermoautotrophicum strain ΔH. *Biochim. Biophys. Acta BBA - Gen. Subj.* **1073**, 77–84 (1991).

[106] C. Zirngibl, W. Dongen, B. Schworer, R. Bunau, M. Richter, A. Klein, R. K. Thauer, H2-forming methylenetetrahydromethanopterin dehydrogenase, a novel type of hydrogenase without iron-sulfur clusters in methanogenic archaea. *Eur. J. Biochem.* **208**, 511–520 (1992).

[107] E. J. Lyon, S. Shima, G. Buurman, S. Chowdhuri, A. Batschauer, K. Steinbach, R. K. Thauer, UV-A/blue-light inactivation of the 'metal-free' hydrogenase (Hmd) from methanogenic archaea. *Eur. J. Biochem.* **271**, 195–204 (2004).

[108] G. C. Hartmann, A. R. Klein, M. Linder, R. K. Thauer, Purification, properties and primary structure of H2-formingN5,N10-methylenetetrahydromethanopterin dehydrogenase from Methanococcus thermolithotrophicus. *Arch. Microbiol.* **165**, 187–193 (1996).

[109] K. Ma, R. K. Thauer, Purification and properties of N5, N10-methylenetetrahydromethanopterin reductase from Methanobacterium thermoautotrophicum (strain Marburg). *Eur. J. Biochem.* **191**, 187–193 (1990).

[110] B. W. te Brömmelstroet, W. J. Geerts, J. T. Keltjens, C. van der Drift, G. D. Vogels, C. van der Drift, G. D. Vogels, Purification and properties of 5,10-methylenetetrahydromethanopterin dehydrogenase and 5,10-methylenetetrahydromethanopterin reductase, two coenzyme F420-dependent enzymes, from Methanosarcina barkeri. *Biochim. Biophys. Acta BBA - Protein Struct. Mol. Enzymol.* **1079**, 293–302 (1991).

[111] T. Lienard, B. Becher, M. Marschall, S. Bowien, G. Gottschalk, Sodium Ion Translocation by N5-Methyltetrahydromethanopterin: Coenzyme M Methyltransferase from Methanosarcina mazei Go1 Reconstituted in Ether Lipid Liposomes. *Eur. J. Biochem.* **239**, 857–864 (1996).

[112] V. R. Vepachedu, J. G. Ferry, Role of the Fused Corrinoid/Methyl Transfer Protein CmtA during CO-Dependent Growth of Methanosarcina acetivorans. *J. Bacteriol.* **194**, 4161–4168 (2012).

[113] S. Rospert, R. Böcher, S. Albracht, R. Thauer, Methyl-coenzyme M reductase preparations with high specific activity from H2-preincubated cells of Methanobacterium thermoautotrophicum. *FEBS Lett.* **291**, 371–375 (1991).

[114] M. Dey, X. Li, R. C. Kunz, S. W. Ragsdale, Detection of Organometallic and Radical Intermediates in the Catalytic Mechanism of Methyl-Coenzyme M Reductase Using the Natural

Substrate Methyl-Coenzyme M and a Coenzyme B Substrate Analogue. *Biochemistry* **49**, 10902–10911 (2010).

[115] P. E. Rouvière, T. A. Bobik, R. S. Wolfe, Reductive activation of the methyl coenzyme M methylreductase system of Methanobacterium thermoautotrophicum delta H. *J. Bacteriol.* **170**, 3946–52 (1988).

[116] J. Ellermann, S. Rospert, R. K. Thauer, M. Bokranz, A. Klein, M. Voges, A. Berkessel, Methyl-coenzyme-M reductase from Methanobacterium thermoautotrophicum (strain Marburg). Purity, activity and novel inhibitors. *Eur. J. Biochem.* **184**, 63–68 (1989).

[117] J. A. Fox, D. J. Livingston, W. H. Orme-Johnson, C. T. Walsh, 8-Hydroxy-5-deazaflavin-reducing hydrogenase from Methanobacterium thermoautotrophicum: 1. Purification and characterization. *Biochemistry* **26**, 4219–4227 (1987).

[118] E. Setzke, R. Hedderich, S. Heiden, R. K. Thauer, H2: Heterodisulfide oxidoreductase complex from Methanobacterium thermoautotrophicum. Composition and properties. *Eur. J. Biochem. FEBS* **220**, 139–48 (1994).

[119] J. Meuer, S. Bartoschek, J. Koch, A. Kunkel, R. Hedderich, Purification and catalytic properties of Ech hydrogenase from Methanosarcina barkeri. *Eur. J. Biochem.* **265**, 325–335 (1999).

[120] R. Hedderich, A. Berkessel, R. K. Thauer, Purification and properties of heterodisulfide reductase from Methanobacterium thermoautotrophicum (strain Marburg). *Eur. J. Biochem.* **193**, 255–261 (1990).

[121] D. R. Lovley, S. Goodwin, Hydrogen concentrations as an indicator of the predominant terminal electron-accepting reactions in aquatic sediments. *Geochim. Cosmochim. Acta* **52**, 2993–3003 (1988).

[122] P. C. Novelli, A. R. Michelson, M. I. Scranton, G. T. Banta, J. E. Hobbie, R. W. Howarth, Hydrogen and acetate cycling in two sulfate-reducing sediments: Buzzards Bay and Town Cove, Mass. *Geochimica et Cosmochimica Acta* **52**, 2477–2486 (1988).

[123] T. M. Hoehler, M. J. Alperin, D. B. Albert, C. S. Martens, Thermodynamic control on hydrogen concentrations in anoxic sediments. *Geochim. Cosmochim. Acta* **62**, 1745–1756 (1998).

[124] G.-C. Zhuang, V. B. Heuer, C. S. Lazar, T. Goldhammer, J. Wendt, V. A. Samarkin, M. Elvert, A. P. Teske, S. B. Joye, K.-U. Hinrichs, Relative importance of methylotrophic methanogenesis in sediments of the Western Mediterranean Sea. *Geochim. Cosmochim. Acta* **224**, 171–186 (2018).

[125] A. Ijiri, F. Inagaki, Y. Kubo, R. R. Adhikari, S. Hattori, T. Hoshino, H. Imachi, S. Kawagucci, Y. Morono, Y. Ohtomo, S. Ono, S. Sakai, K. Takai, T. Toki, D. T. Wang, M. Y. Yoshinaga, G. L. Arnold, J. Ashi, D. H. Case, T. Feseker, K.-U. Hinrichs, Y. Ikegawa, M. Ikehara, J. Kallmeyer, H. Kumagai, M. A. Lever, S. Morita, K.-i. Nakamura, Y. Nakamura, M. Nishizawa, V. J. Orphan, H. Røy, F. Schmidt, A. Tani, W. Tanikawa, T. Terada, H. Tomaru, T. Tsuji, U. Tsunogai, Y. T. Yamaguchi, N. Yoshida, Deep-biosphere methane production stimulated by geofluids in the Nankai accretionary complex. *Sci. Adv.* **4**, eaao4631 (2018).

[126] R. H. Michener, M. I. Scranton, P. Novelli, Hydrogen (H2) distributions in the carmans river estuary. *Estuarine, Coastal and Shelf Science* **27**, 223–235 (1988).

[127] H. Yao, R. Conrad, Thermodynamics of methane production in different rice paddy soils from China, the Philippines and Italy. *Soil Biology and Biochemistry* **31**, 463–473 (1999).

[128] T. M. Hoehler, M. J. Alperin, D. B. Albert, C. S. Martens, Field and laboratory studies of methane oxidation in an anoxic marine sediment: Evidence for a methanogen-sulfate reducer consortium. *Glob. Biogeochem. Cycles* **8**, 451–463 (1994).

[129] G. E. Claypool, A. V. Milkov, Y. J. Lee, M. E. Torres, W. S. Borowski, H. Tomaru, Microbial methane generation and gas transport in shallow sediments of an accretionary complex, southern hydrate ridge (ODP Leg 204), offshore Oregon, USA. *Proc. Ocean Drill. Program Sci. Results* **204** (2006).

[130] O. Sivan, D. P. Schrag, R. W. Murray, Rates of methanogenesis and methanotrophy in deep-sea sediments. *Geobiology* **5**, 141–151 (2007).

[131] R. J. Parkes, B. A. Cragg, N. Banning, F. Brock, G. Webster, J. C. Fry, E. Hornibrook, R. D. Pancost, S. Kelly, N. Knab, B. B. Jørgensen, J. Rinna, A. J. Weightman, Biogeochemistry and biodiversity of methane cycling in subsurface marine sediments (Skagerrak, Denmark). *Environ. Microbiol.* **9**, 1146–1161 (2007).

[132] F. Beulig, H. Røy, S. E. McGlynn, B. B. Jørgensen, Cryptic CH4 cycling in the sulfate–methane transition of marine sediments apparently mediated by ANME-1 archaea. *ISME J.* **13**, 250–262 (2018).

[133] P.-C. Chuang, T. Frank Yang, K. Wallmann, R. Matsumoto, C.-Y. Hu, H.-W. Chen, S. Lin, C.-H. Sun, H.-C. Li, Y. Wang, A. W. Dale, Carbon isotope exchange during anaerobic oxidation of methane (AOM) in sediments of the northeastern South China Sea. *Geochim. Cosmochim. Acta* **246**, 138–155 (2018).

[134] P. Schönheit, H. J. Perski, ATP synthesis driven by a potassium diffusion potential in Methanobacterium thermoautotrophicum is stimulated by sodium. *FEMS Microbiol. Lett.* **20**, 263–267 (1983).

[135] E. Heine-Dobbernack, S. M. Schoberth, H. Sahm, Relationship of Intracellular Coenzyme F(420) Content to Growth and Metabolic Activity of Methanobacterium bryantii and Methanosarcina barkeri. *Appl. Environ. Microbiol.* **54**, 454–9 (1988).

[136] R. Sander, Compilation of Henry's law constants (version 4.0) for water as solvent. *Atmospheric Chem. Phys.* **15**, 4399–4981 (2015).

[137] A. M. Feist, J. C. M. Scholten, B. Ø. Palsson, F. J. Brockman, T. Ideker, Modeling methanogenesis with a genome-scale metabolic reconstruction of Methanosarcina barkeri. *Mol. Syst. Biol.* **2**, 2006.0004 (2006).

[138] M. Whiticar, E. Faber, M. Schoell, Biogenic methane formation in marine and freshwater environments: CO2 reduction vs. acetate fermentation—Isotope evidence. *Geochim. Cosmochim. Acta* **50**, 693–709 (1986).

[139] J. McIntosh, A. Martini, S. Petsch, R. Huang, K. Nüsslein, Biogeochemistry of the Forest City Basin coalbed methane play. *International Journal of Coal Geology* **76**, 111–118 (2008).

[140] M. F. Kirk, B. H. Wilson, K. A. Marquart, L. H. Zeglin, D. S. Vinson, T. M. Flynn, Solute concentrations influence microbial methanogenesis in coal-bearing strata of the Cherokee basin, USA. *Front. Microbiol.* **6** (2015).

[141] J. C. McIntosh, L. M. Walter, A. M. Martini, Pleistocene recharge to midcontinent basins: Effects on salinity structure and microbial gas generation. *Geochimica et Cosmochimica Acta* **66**, 1681–1700 (2002).

[142] D. Strapoć, M. Mastalerz, A. Schimmelmann, A. Drobniak, S. Hedges, Variability of geochemical properties in a microbially dominated coalbed gas system from the eastern margin of the Illinois Basin, USA. *International Journal of Coal Geology* **76**, 98–110 (2008).

[143] M. E. Schlegel, J. C. McIntosh, B. L. Bates, M. F. Kirk, A. M. Martini, Comparison of fluid geochemistry and microbiology of multiple organic-rich reservoirs in the Illinois Basin, USA: Evidence for controls on methanogenesis and microbial transport. *Geochimica et Cosmochimica Acta* **75**, 1903–1919 (2011).

[144] R. M. Flores, C. A. Rice, G. D. Stricker, A. Warden, M. S. Ellis, Methanogenic pathways of coal-bed gas in the Powder River Basin, United States: The geologic factor. *Int. J. Coal Geol.* **76**, 52–75 (2008).

[145] B. L. Bates, J. C. McIntosh, K. A. Lohse, P. D. Brooks, Influence of groundwater flowpaths, residence times and nutrients on the extent of microbial methanogenesis in coal beds: Powder River Basin, USA. *Chemical Geology* **284**, 45–61 (2011).

[146] K. A. Baublys, S. K. Hamilton, S. D. Golding, S. Vink, J. Esterle, Microbial controls on the origin and evolution of coal seam gases and production waters of the Walloon Subgroup; Surat Basin, Australia. *International Journal of Coal Geology* **147–148**, 85–104 (2015).

[147] R. Aravena, S. Harrison, J. Barker, H. Abercrombie, D. Rudolph, Origin of methane in the Elk Valley coalfield, southeastern British Columbia, Canada. *Chem. Geol.* **195**, 219–227 (2003).

[148] N. Riedinger, M. J. Formolo, T. W. Lyons, S. Henkel, A. Beck, S. Kasten, An inorganic geochemical argument for coupled anaerobic oxidation of methane and iron reduction in marine sediments. *Geobiology* **12**, 172–181 (2014).

[149] T. Giunta, E. D. Young, O. Warr, I. Kohl, J. L. Ash, A. Martini, S. O. Mundle, D. Rumble, I. Pérez-Rodríguez, M. Wasley, D. E. LaRowe, A. Gilbert, B. Sherwood Lollar, Methane sources and sinks in continental sedimentary systems: New insights from paired clumped isotopologues 13CH3D and 12CH2D2. *Geochim. Cosmochim. Acta* **245**, 327–351 (2019).

[150] T. Giunta, J. Labidi, I. E. Kohl, L. Ruffine, J. P. Donval, L. Géli, M. N. Çağatay, H. Lu, E. D. Young, Evidence for methane isotopic bond re-ordering in gas reservoirs sourcing cold seeps from the Sea of Marmara. *Earth and Planetary Science Letters* **553**, 116619 (2021).

[151] D. S. Vinson, N. E. Blair, D. J. Ritter, A. M. Martini, J. C. McIntosh, Carbon mass balance, isotopic tracers of biogenic methane, and the role of acetate in coal beds: Powder River Basin (USA). *Chemical Geology* **530**, 119329 (2019).

[152] H. Schweitzer, D. Ritter, J. McIntosh, E. Barnhart, A. B. Cunningham, D. Vinson, W. Orem, M. W. Fields, Changes in microbial communities and associated water and gas geochemistry

across a sulfate gradient in coal beds: Powder River Basin, USA. *Geochimica et Cosmochimica Acta* **245**, 495–513 (2019).

[153] A. M. Martini, L. M. Walter, J. M. Budai, T. C. W. Ku, C. J. Kaiser, M. Schoell, Genetic and temporal relations between formation waters and biogenic methane: Upper Devonian Antrim Shale, Michigan Basin, USA. *Geochimica et Cosmochimica Acta* **62**, 1699–1720 (1998).

[154] A. M. Martini, L. M. Walter, T. C. W. Ku, J. M. Budai, J. C. McIntosh, M. Schoell, Microbial production and modification of gases in sedimentary basins: A geochemical case study from a Devonian shale gas play, Michigan basin. *AAPG Bulletin* **87**, 1355–1375 (2003).

[155] P. D. Jenden, I. R. Kaplan, Comparison of microbial* gases from the Middle America Trench and Scripps Submarine Canyon: Implications for the origin of natural gas. *Applied Geochemistry* **1**, 631–646 (1986).

[156] U. Berner, M. Von Breymann, E. Faber, P. Bertrand, *Bacterial Gas* (1992), pp. 147–156.